AGU ADVANCING EARTH AND SPACE SCIENCES

Water Resources Research

RESEARCH ARTICLE
10.1029/2023WR034664

Pore-Scale Modeling of PFAS Transport in Water-Unsaturated Porous Media: Air–Water Interfacial Adsorption and Mass-Transfer Processes in Thin Water Films

Sidian Chen[1] **and Bo Guo**[1]

[1]Department of Hydrology and Atmospheric Sciences, University of Arizona, Tucson, AZ, USA

Abstract Air–water interfacial adsorption complicates per- and polyfluoroalkyl substance (PFAS) transport in vadose zones. Air–water interfaces can arise from pendular rings between soil grains and thin water films on grain surfaces, the latter of which account for over 90% of the total air–water interfaces for most field-relevant conditions. However, whether all thin-water-film air–water interfaces are accessible by PFAS and how mass-transfer limitations in thin water films control PFAS transport in soils remain unknown. We develop a pore-scale model that represents both PFAS adsorption at bulk capillary and thin-water-film air–water interfaces and the mass-transfer processes between bulk capillary water and thin water films (including advection, aqueous diffusion, and surface diffusion along air–water interfaces). We apply the pore-scale model to a series of numerical experiments—constrained by experimentally determined hydraulic parameters and air–water interfacial area data sets—to examine the impact of thin-water-film mass-transfer limitations in a sand medium. Our analyses suggest: (a) The mass-transfer limitations between bulk capillary water and thin water films inside a pore are negligible due to surface diffusion. (b) However, strong mass-transfer limitations arise in thin water films of pore clusters where pendular rings disconnect. The mass-transfer limitations lead to early arrival and long tailing behaviors even if surface diffusion is present. (c) Despite the mass-transfer limitations, all air–water interfaces in the thin water films were accessed by PFAS under the simulated conditions. These findings highlight the importance of incorporating the thin-water-film mass-transfer limitations and surface diffusion for modeling PFAS transport in vadose zones.

Key Points:

- We develop a pore-scale modeling framework for simulating per- and polyfluoroalkyl substance (PFAS) transport in water-unsaturated porous media
- The model accounts for air—water interfacial adsorption and mass-transfer processes in thin water films including surface diffusion
- Thin-water-film mass-transfer limitations cause significant early arrival and long tailing in PFAS breakthrough curves

Supporting Information:

Supporting Information may be found in the online version of this article.

Correspondence to:

B. Guo,
boguo@arizona.edu

Citation:

Chen, S., & Guo, B. (2023). Pore-scale modeling of PFAS transport in water-unsaturated porous media: Air–water interfacial adsorption and mass-transfer processes in thin water films. *Water Resources Research*, *59*, e2023WR034664. https://doi.org/10.1029/2023WR034664

Received 12 FEB 2023
Accepted 4 AUG 2023

Author Contributions:

Conceptualization: Bo Guo
Data curation: Sidian Chen
Formal analysis: Sidian Chen, Bo Guo
Funding acquisition: Bo Guo
Investigation: Sidian Chen
Methodology: Sidian Chen, Bo Guo
Project Administration: Bo Guo
Resources: Bo Guo
Software: Sidian Chen
Supervision: Bo Guo
Validation: Sidian Chen
Visualization: Sidian Chen
Writing – original draft: Sidian Chen
Writing – review & editing: Bo Guo

1. Introduction

Per- and polyfluoroalkyl substances (PFAS) are emerging contaminants widely dispersed in the environment. Many field observations have demonstrated that PFAS accumulate in vadose zones and act as a long-term contamination source to the groundwater underneath (Adamson et al., 2020; Anderson et al., 2019, 2022; Brusseau, Anderson, & Guo, 2020; Dauchy et al., 2019; Filipovic et al., 2015; Quinnan et al., 2021; Schaefer et al., 2022; Weber et al., 2017; Xiao et al., 2015). Most PFAS are surfactants that adsorb at solid–water (Higgins & Luthy, 2006; Van Glubt et al., 2021; Wei et al., 2017) and air–water interfaces (Brusseau, 2018; Brusseau, Khan, et al., 2019; Costanza et al., 2019; Lyu et al., 2018; Schaefer, Drennan, et al., 2019; Silva et al., 2019; Stults et al., 2022). In particular, adsorption at air–water interfaces has been shown to be a primary mechanism responsible for the strong retention of PFAS in vadose zones (e.g., Brusseau, 2018; Guo et al., 2020; Schaefer et al., 2022). Effective characterization and remediation of PFAS contamination sites will require a comprehensive understanding of PFAS adsorption and retention processes at the air–water interfaces in vadose zones.

In the vadose zone, air–water interfaces arise from pendular rings between soil grains (referred to as "bulk capillary air–water interfaces" hereafter) and thin water films on grain surfaces (referred to as "thin-water-film air–water interfaces" hereafter) (see Figure 1). At near water-saturated conditions, the bulk capillary air–water interfaces are greater than the thin-water-film air–water interfaces. As the water saturation decreases, the bulk capillary air–water interfaces first increase and then decrease (Araujo & Brusseau, 2020; Dalla et al., 2002; Kibbey & Chen, 2012; Porter et al., 2009; Reeves & Celia, 1996). Conversely, the thin-water-film air–water interfaces increase monotonically as the water saturation decreases and quickly become the dominant air–water interfaces (Brusseau et al., 2007; Costanza-Robinson & Brusseau, 2002; Kibbey & Chen, 2012). When soil grain surfaces contain significant microscale roughness, thin-water-film air–water interfaces are much greater than that for smooth surfaces under the same capillary pressure or matric potential. The dominance of thin-water-film air–water interfaces in unsaturated porous media has been confirmed by many studies (Brusseau et al., 2006, 2007;

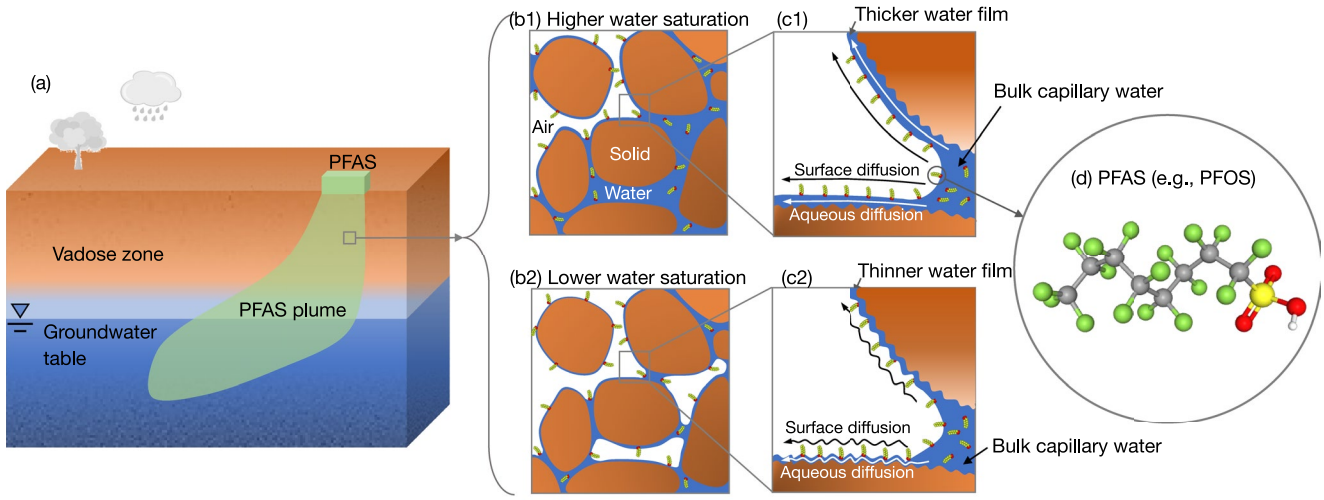

Figure 1. (a) Schematic for per- and polyfluoroalkyl substances (PFAS) contamination in the vadose zone and groundwater, (b) adsorption of PFAS at air–water interfaces arising from bulk capillary water and thin water films in soils under different wetting conditions, (c) mass transfer of PFAS between bulk capillary water and thin water films, and (d) an example PFAS molecule (e.g., PFOS), where the colors denote different atoms: gray–carbon, green–fluorine, red–oxygen, yellow–sulfur, and white–hydrogen. In panel (d), the molecule consists of a hydrophobic and oleophobic tail (the fluorocarbon chain on the left) and a hydrophilic head (the sulfonic acid functional group on the right).

Costanza-Robinson & Brusseau, 2002; Jiang et al., 2020b; Kibbey & Chen, 2012; Or & Tuller, 1999). For example, Brusseau et al. (2007) reported that thin-water-film air–water interfaces account for more than 90% of the total air–water interfaces for a sand at a water saturation over 0.5, which is even greater than the water saturation in most sandy vadose zones. Given that air–water interfaces contribute significantly to PFAS retention, the dominant thin-water-film air–water interfaces are expected to act as a primary factor controlling PFAS transport in vadose zones.

However, it remains unknown whether all thin-water-film air–water interfaces can be accessed by PFAS. Prior studies—using interfacially active tracers (not PFAS) to measure the air–water interfacial area—have demonstrated that the liquid-phase interfacial partitioning tracers may not access all the thin-water-film air–water interfaces under certain experimental conditions (Costanza-Robinson & Brusseau, 2002; Kibbey & Chen, 2012). For instance, Costanza-Robinson and Brusseau (2002) found that the air–water interfacial areas measured by liquid-phase interfacial partitioning tracers are much smaller than those by gas-phase interfacial partitioning tracers under drier conditions. They hypothesized that the discrepancy was caused by the gas-phase interfacial partitioning tracers having accessed additional thin-water-film air–water interfaces. Kibbey and Chen (2012) studied the air–water interfacial areas measured by different liquid-phase interfacial partitioning tracer methods using a pore-network modeling approach and suggested that the liquid-phase interfacial partitioning tracers may not access all thin-water-film air–water interfaces under certain experimental transport conditions such as miscible displacement experiments.

Like the non-PFAS interfacially active tracers, it is possible that PFAS may only access a fraction of the thin-water-film air–water interfaces under certain transport conditions. Recent mathematical modeling of PFAS transport using the total air–water interfacial area determined by liquid-phase interfacial partitioning tracers agrees well with measured breakthrough curves (e.g., Brusseau, 2020; Brusseau, Khan, et al., 2019; Guo et al., 2022; Ji et al., 2021; Van Glubt et al., 2021; Zeng et al., 2021). It was suggested that the air–water interfacial area measured by liquid-phase interfacial partitioning tracers is representative for modeling PFAS transport in the water-unsaturated sand (Brusseau & Guo, 2021). However, those transport experiments were conducted at relatively large water saturation—all of them were greater than 0.6 except for one data set that used a water saturation of approximately 0.4 (Lyu et al., 2020). While the thin-water-film air–water interfaces are more accessible at higher water saturation (Brusseau, 2020; Brusseau, Yan, et al., 2019; Guo et al., 2022; Ji et al., 2021; Stults et al., 2022; Zeng et al., 2021), they may not be fully accessible at drier conditions. As water saturation decreases, the pendular rings between soil grains disconnect and the bulk water between pores is only connected by thin water films (see Figure 1b) (Vanapalli et al., 1998; Wan & Tokunaga, 1997). Concomitantly, the water films

become much thinner as the water saturation in the soil medium decreases (down to <100 nm) (see Figure 1c) (Tokunaga, 2011). Additionally, thin water films become more curved following the microscale topography on rough grain surfaces under drier conditions, which significantly increases the length of thin water films (see Figure 1c) (Jiang et al., 2020a, 2020b; Zheng et al., 2015). These three factors collectively increase the time scale of mass transfer in thin water films and may substantially reduce the accessibility of thin-water-film air–water interfaces by PFAS.

An important phenomenon that has not been discussed in the hydrology literature is that PFAS adsorbed at air–water interfaces may also move along the interfaces driven by molecular diffusion (see Figure 1c), which can act as a critical additional mass-transfer process. Diffusion of adsorbed hydrocarbon surfactants at air–water interfaces have been reported in the surface science literature (often referred to as surface diffusion) (Karakashev & Ivanova, 2010; Stoyanov & Denkov, 2001; Valkovska & Danov, 2000, 2001). As shown by these studies, the surface diffusivity of hydrocarbon surfactants at air–water interfaces is close to that of the aqueous diffusivity. However, unlike the aqueous diffusion, surface diffusion does not scale with the film thickness—the surface diffusion flux does not decrease in thinner water films. Furthermore, for the interfacially active PFAS especially those with longer carbon chains and greater interfacial activity, the adsorbed mass at the air–water interfaces may represent the majority of their mass in a thin water film, especially when the thickness of the water films is down to <100 nm. Therefore, surface diffusion along the air–water interfaces is likely to become the dominant mass-transfer process for PFAS in thin water films. Yet, surface diffusion along the air–water interfaces has been overlooked—To our knowledge, it has not been considered in any of the prior work that used interfacially active tracers to measure air–water interfacial area nor in the recent literature of PFAS transport in the vadose zone. We hypothesize that surface diffusion may greatly enhance the accessibility of thin-water-film air–water interfaces and is a critical process that needs to be represented for quantifying PFAS transport in the vadose zone, especially under drier conditions.

The objective of the present study is to examine the accessibility of thin-water-film air–water interfaces without and with the presence of the surface diffusion of PFAS adsorbed at air–water interfaces, and the impact of mass-transfer limitations in thin water films on PFAS transport in water-unsaturated porous media. To achieve this objective, we develop a new pore-scale model that represents PFAS adsorption at bulk capillary and thin-water-film air–water interfaces and solid–water interfaces, and mass-transfer processes in thin water films including the surface diffusion of PFAS adsorbed at air–water interfaces. Constrained by experimentally determined hydraulic parameters and air–water interfacial area data sets, we conduct a series of numerical experiments to examine the impact of thin-water-film mass-transfer limitations on PFAS transport in a water-unsaturated sand medium.

2. Pore-Network Modeling Framework

We develop a pore-scale modeling framework to represent the various retention and transport processes of PFAS in water–unsaturated porous media. The pore-scale modeling is built upon the spirit of pore-network models which have been widely used and shown to be reliable for pore-scale simulations of both passive and reactive solute transport (e.g., Bijeljic & Blunt, 2006; Bijeljic et al., 2004; Hasan et al., 2019; Kibbey & Chen, 2012; Li et al., 2006; Mehmani et al., 2014; Mehmani & Tchelepi, 2017; Oostrom et al., 2016; Qin et al., 2016; Qin & Hassanizadeh, 2015; Raoof et al., 2010; Raoof & Hassanizadeh, 2013; Yang et al., 2016). We present our new pore-network modeling framework below, including the pore-network representation, mathematical formulations, and numerical methods. A complete list of notations used in describing the mathematical formulations is provided in Notation.

2.1. Constructing Pore Networks to Represent the Soil Pore Structures

We represent the pore structure in a porous medium with a three-dimensional unstructured pore network, which can be constructed using a network generation algorithm (Qin & van Brummelen, 2019). Figure 2a shows an example pore network generated using the algorithm of Qin and van Brummelen (2019). The pore network can be calibrated to represent a specific porous medium using experimental data such as soil water characteristics and air–water interfacial area as a function of water saturation. We assign all the void volumes to pore bodies, which are represented by cubes (Joekar-Niasar et al., 2010; Thompson, 2002; Weishaupt et al., 2022; Weishaupt & Helmig, 2021). The pore bodies are connected by square-tube pore throats (see Figure 2b). The pore throats

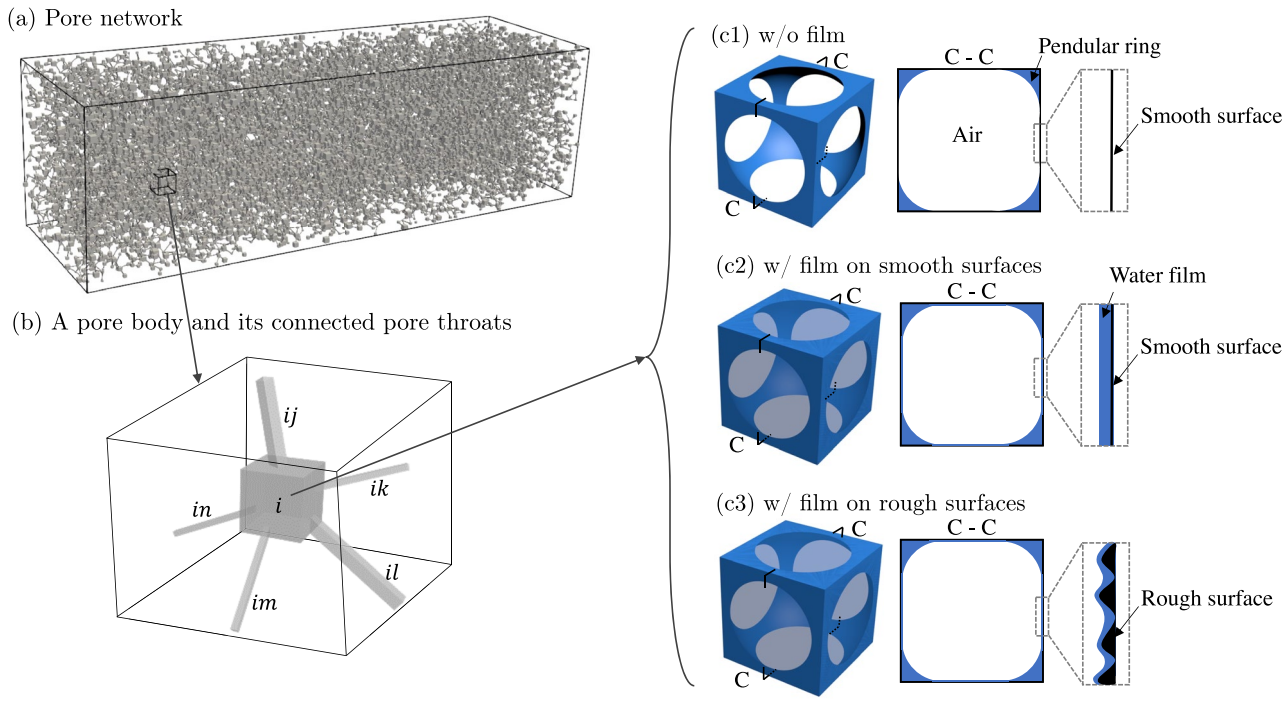

Figure 2. (a) An example three-dimensional unstructured pore network constructed using a network-generation algorithm, (b) a zoom-in view of a pore body *i* and its connected pore throats in the pore network, and (c1–c3) the configuration of air–water interfaces in a water-unsaturated pore body *i*. Panel (c1) shows a pore body with only bulk capillary air–water interfaces in the corners and edges (no water films are present), and panel (c2) and panel (c3) show pore bodies with both bulk capillary and thin-water-film air–water interfaces. The pore walls in panel (c2) are smooth while those in panel (c3) contain microscale surface roughness.

are assumed volumeless and only provide hydraulic conductance for bulk capillary water and thin water films. We assume that only the air–water interfaces in the pore bodies contribute to the interfacial adsorption of PFAS. The pore walls are assumed water-wet with a zero contact angle.

2.2. Modeling Air–Water Configuration and Unsaturated Water Flow in a Pore Network

2.2.1. Modeling Pore-Scale Air–Water Configuration

We use the percolation theory (Broadbent & Hammersley, 1957; Frisch & Hammersley, 1963; Wilkinson & Willemsen, 1983) to determine the pore-scale air–water configuration in the pore network at different water saturations, as has been commonly done in the quasi-static pore-network modeling literature (e.g., Blunt, 2001; Celia et al., 1995). The pore network is initially filled by water. We gradually increase the air pressure at the inlet to displace the resident water by air. After air invades a pore body, the remaining water occupies part of the pore body as bulk capillary water at the corners and edges, and as water films on the solid surfaces (see Figure 2c). A pore throat provides full conductance for bulk water before air invasion. After air invasion, a pore throat provides conductance for bulk capillary water at the edges and for water films on the solid surfaces. In a soil medium, the bulk capillary water (i.e., pendular rings) between soil grains may become disconnected and trapped therein under drier conditions. We represent the disconnect of bulk water by removing the conductance for bulk capillary water in the pore throats that connect the pore bodies where the bulk capillary water is disconnected. Those pore bodies are identified by comparing their capillary pressure to a threshold capillary pressure $p^c_{cr,i}$ at which the discontinuity occurs. The threshold pressure for each pore body *i* is determined by assuming packed uniform spheres, which is given by (Wan & Tokunaga, 1997)

$$p^c_{cr,i} = \frac{9.068\sigma}{2r_i}, \tag{1}$$

where σ is the surface tension and r_i is the radius of the inscribed sphere of pore body *i*. Once the capillary pressure in a pore body *i* goes above $p^c_{cr,i}$, the bulk water in the pore body is trapped.

2.2.2. Modeling Unsaturated Water Flow in the Pore Network

We consider steady-state water flow in the water-unsaturated pore network derived from Section 2.2.1. The pore-scale air–water configuration remains unchanged over time. For each pore body i, the water phase is governed by the following mass balance equation

$$\sum_{j=1}^{n_i}\left(\delta_{ij}q_{w,ij}^{b}+q_{w,ij}^{f}\right)=0, \tag{2}$$

where $j=1,2,\ldots,n_i$ are the pore bodies that connect to pore body i (n_i is the coordination number of pore body i), $q_{w,ij}^{b}$ is the bulk capillary water flux between pore body i and j, δ_{ij} is a Boolean function to account for the removal of bulk capillary water conductance in pore throat ij where the bulk capillary water is disconnected (i.e., $\delta_{ij}=0$ if the bulk capillary water is disconnected in pore body i or j; otherwise, $\delta_{ij}=1$), and $q_{w,ij}^{f}$ is the water flux through the thin water films between pore body i and j. Assuming that the bulk capillary water follows the Stokes flow with no friction between air and water, $q_{w,ij}^{b}$ can be computed as

$$q_{w,ij}^{b}=G_{w,ij}^{b}(p_{w,i}-p_{w,j}), \tag{3}$$

where $G_{w,ij}^{b}$ is the bulk capillary water conductance in pore throat ij, which can be obtained from the relationship between the water conductance and the water configuration in the pore throat determined by computational fluid dynamics simulations (see e.g., Equations 9–16 in Chen et al. (2020)); $p_{w,i}$ and $p_{w,j}$ are the water pressures in pore bodies i and j, respectively. Similarly, assuming the thin-water-film water flow follows the Stokes flow with no friction between air and water, $q_{w,ij}^{f}$ is given by

$$q_{w,ij}^{f}=G_{w,ij}^{f}(p_{w,i}-p_{w,j}), \tag{4}$$

where $G_{w,ij}^{f}$ is the thin-water-film water conductance. $G_{w,ij}^{f}=0$ if pore throat ij is water-saturated. If pore throat ij is water-unsaturated, $G_{w,ij}^{f}$ can be computed as (Tuller & Or, 2001)

$$G_{w,ij}^{f}=\frac{\left(h_{ij}^{f}\right)^{3}L_{aw,ij}^{f}}{3\mu l_{ij}^{f}}, \tag{5}$$

where h_{ij}^{f} is the thickness of thin water films in pore throat ij (see Section 2.3.2 for the calculation of h_{ij}^{f}), $L_{aw,ij}^{f}$ is the length of the thin water film (i.e., thin-water-film air–water interface) along the cross-section of pore throat ij, μ is the viscosity of water, l_{ij}^{f} is the length of the thin water film between pore bodies i and j (see Section 2.3.2 for the calculation of l_{ij}^{f}).

2.3. Modeling PFAS Transport in a Water–Unsaturated Pore Network

We consider PFAS transport in the water-unsaturated pore network derived from Sections 2.1 and 2.2. We first compute the areas of air–water and solid–water interfaces (Section 2.3.1). Then, we present governing equations for interfacial adsorption and transport (i.e., advection, aqueous diffusion, and surface diffusion) of PFAS in the water-unsaturated pore network (Section 2.3.2).

2.3.1. Calculating the Areas of Air–Water and Solid–Water Interfaces

PFAS in a water-unsaturated porous medium may access both the bulk capillary and thin-water-film air–water interfaces. We compute both types of air–water interfaces below. To be consistent with the transport models (Section 2.3.2) that separate the thin water films from the bulk capillary water, we also separate the solid–water interfaces to those covered by bulk capillary water and those covered by thin water films—we refer to the former as bulk capillary solid–water interfaces and the latter as thin-water-film solid–water interfaces.

2.3.1.1. Areas of Bulk Capillary Air–Water and Solid–Water Interfaces

For a water-saturated pore body i, no air–water interfaces exist. Thus the bulk capillary air–water interfacial area is $a_{aw,i}^{b}=0$. The area of solid–water interfaces $\left(a_{sw,i}^{b}\right)$ is equal to the solid surface area of the pore body

$$a_{sw,i}^{b}=24X_{i}r_{i}^{2}, \tag{6}$$

where X_i is the surface roughness factor, which is defined as the ratio between the area of solid–water interfaces in the presence of microscale surface roughness and that when assuming a smooth solid surface.

For a water–unsaturated pore body i, water resides at the corners and edges of the cube, forming bulk capillary air–water interfaces as menisci (see Figure 2c). Denoting the capillary pressure in the pore body by p_i^c, the radii of the menisci at the corners (denoted by $r_{i,c}$) and those at the edges (denoted by $r_{i,e}$) can be computed via the Young-Laplace equation as $r_{i,c} = 2\sigma/p_i^c$ and $r_{i,e} = \sigma/p_i^c$, respectively. The areas of menisci at the corners and at the edges are $4\pi r_{i,c}^2$ and $12\pi r_{i,e}(r_i - r_{i,c})$, respectively. An additional type of meniscus may arise at the intersection between a water-unsaturated pore body i and its neighboring water-saturated pore throats. This type of meniscus is often referred to as the main terminal meniscus. Suppose pore throat ij is water-saturated, the area of the main terminal meniscus is equal to $8\pi r_{i,e}^2\left(1 - \sqrt{1 - (r_{ij}/r_{i,c})^2}\right)$, where r_{ij} is the radius of the inscribed circle of the cross-section of pore throat ij. Summing the three areas gives the total area of bulk capillary air–water interfaces in pore body i

$$a_{aw,i}^b = 4\pi r_{i,c}^2 + 12\pi r_{i,e}(r_i - r_{i,c}) + \sum_{j=1}^{n_i'} 8\pi r_{i,e}^2\left(1 - \sqrt{1 - (r_{ij}/r_{i,c})^2}\right), \tag{7}$$

where $j = 1, 2, \ldots, n_i'$ are the pore bodies connected to pore body i through water-saturated pore throat ij, n_i' is the number of water-saturated pore throats connected to pore body i. The area of the solid–water interfaces covered by the bulk capillary water at the corners and edges of pore body i can be computed as

$$a_{sw,i}^b = X_i\left(24r_i^2 - 6\left(4(r_i - r_{i,e})^2 - (4 - \pi)(r_{i,c} - r_{i,e})^2\right)\right). \tag{8}$$

2.3.1.2. Area of Thin-Water-Film Air–Water and Solid–Water Interfaces

Thin-water-film air–water and solid–water interfaces only arise in water-unsaturated pore bodies. In a water–unsaturated pore body i, thin water films spread on the solid surfaces that are not covered by bulk capillary water, and create thin-water-film air–water and solid–water interfaces. For a solid surface with microscale roughness, the thin-water-film air–water interfacial area will be curved and become significantly greater than those on a smooth surface (see Figure 2c). We need to account for the increased thin-water-film air–water interfacial area due to the presence of surface roughness. Using $X_{l,i}$ to denote the amplification factor representing the ratio between the areas of thin-water-film air–water interfaces on rough and smooth surfaces, we can compute the thin-water-film air–water interfacial area in pore body i as

$$a_{aw,i}^f = 6X_{l,i}\left(4(r_i - r_{i,e})^2 - (4 - \pi)r_{i,c}^2\right). \tag{9}$$

The amplification factor $X_{l,i}$ can be modeled by empirical functions such as the reciprocal function (Zheng et al., 2015) or logistic function (Jiang et al., 2020b) proposed in the literature. Here we employ the logistic function that was demonstrated to match the air-water interfacial area in various soil media measured by gas-phase interfacial partitioning tracer test experiments (Jiang et al., 2020b).

$$X_{l,i} = \frac{X_i + e^{k_i(h_{ad,i} - h_{m,i})}}{1 + e^{k_i(h_{ad,i} - h_{m,i})}}, \tag{10}$$

where k_i and $h_{m,i}$ are fitting parameters that can be determined by comparing to experimentally measured air–water interfacial areas, $h_{ad,i}$ is the thickness of absorptive film on smooth surfaces (Iwamatsu & Horii, 1996)

$$h_{ad,i} = \left(\frac{A_{svl}}{6\pi p_i^c}\right)^{1/3}, \tag{11}$$

where A_{svl} is the Hamaker constant that is a function of the solid surface materials and is available in the literature for a variety of solid surfaces (Or & Tuller, 1999).

The area of solid–water interfaces covered by the thin water films can be determined as

$$a_{sw,i}^f = 6X_i\left(4(r_i - r_{i,e})^2 - (4 - \pi)(r_{i,c} - r_{i,e})^2\right). \tag{12}$$

In the present study, we assume that the pore walls of all pore bodies have the same surface roughness, that is, X_i and $X_{l,i}$ are the same across the entire pore network. If detailed information of the surface roughness heterogeneity is available, it can be accounted for by using spatially varying X_i and $X_{l,i}$ in the pore network.

2.3.2. Modeling PFAS Transport in a Water-Unsaturated Pore Network

Within each pore body, PFAS can reside in bulk water, thin water films, solid–water interfaces, and air–water interfaces. They can also transport between neighboring pore bodies via advection, aqueous diffusion, and surface diffusion along air–water interfaces through the bulk capillary water and thin water films in the pore throats. We represent these processes by formulating mass balance equations coupled with flux equations for each pore body i (which can be either water-unsaturated or water-saturated) in the pore network.

For each water-unsaturated pore body i, we assume PFAS are well-mixed in the bulk capillary water and in the thin water films, respectively. Assuming a well-mixed condition in the bulk capillary water in each pore body was shown to be valid for small to moderate pore-scale Péclet numbers (i.e., $Pe \leq 257$) (Yang et al., 2016). Because PFAS in the two domains may not be in chemical equilibrium, we formulate separate governing equations for PFAS in the bulk capillary water and thin water films and represent the mass transfer between the two domains by a first-order flux driven by aqueous diffusion and surface diffusion along air–water interfaces. The governing equation for PFAS in the bulk capillary water of pore body i can be written as

$$\begin{aligned}&\frac{\partial\left(V_i s_{w,i}^b c_i^b\right)}{\partial t}+\frac{\partial\left(a_{aw,i}^b K_{aw,i}^b c_i^b\right)}{\partial t}+\frac{\partial\left(a_{sw,i}^b K_{sw,i}^b\left(c_i^b\right)^{N_{sw,i}^b}\right)}{\partial t}\\&+\sum_{j=1}^{n_i}\delta_{ij}\left(c_{ij}^b q_{w,ij}^b+a_{w,ij}^b D_0^b\frac{c_i^b-c_j^b}{l_{ij}}+D_{aw}^b L_{aw,ij}^b\frac{K_{aw,i}^b c_i^b-K_{aw,j}^b c_j^b}{l_{ij}}\right)\\&+D_0^f L_{aw,i}^f h_i^f\frac{c_i^b-c_i^f}{l_i^f}+D_{aw}^f L_{aw,i}^f\frac{K_{aw,i}^b c_i^b-K_{aw,i}^f c_i^f}{l_i^f}=0,\end{aligned}\tag{13}$$

where V_i is the volume of the pore body i. Using superscripts b and f to respectively denote the variables for bulk capillary water and thin water films, the variables are defined as follows. $s_{w,i}^b$ is the bulk capillary water saturation. c_i is the aqueous PFAS concentration, c_{ij} is the PFAS concentration in the upstream pore body of i and j (i.e., $c_{ij}=c_i$ if water flows from pore body i to pore body j, while $c_{ij}=c_j$ if water flows from pore body j to pore body i), $a_{w,ij}^b$ is the cross-sectional area of bulk water in the pore throat ij, $K_{aw,i}$ is the air–water interfacial adsorption coefficient, $K_{sw,i}$ and $N_{sw,i}$ are the Freundlich isotherm parameters for the solid-phase adsorption, D_0 is the aqueous molecular diffusion coefficient, D_{aw} is the surface diffusion coefficient which is assumed equal to D_0, l_{ij} is the length of pore throat ij, $L_{aw,i}^f$ is the total length of the interfaces between bulk capillary water and thin water films, and h_i^f is the thin-water-film thickness given by $h_i^f=X_{h,i}h_{ad,i}$ where $X_{h,i}=X_i/X_{l,i}$ (Jiang et al., 2020b; Zheng et al., 2015). l_i^f is the distance from the bulk capillary water to the center of the thin-water film in a face of the cubic pore body which is given by $l_i^f=(r_i-r_{i,e})(X_{l,i})^{1/2}$. Detailed information for the geometrical parameters (e.g., $a_{w,ij}^b$, l_{ij}, $L_{aw,i}^f$, h_i^f, and l_i^f) and their graphical representation is presented in Figure S1 in Supporting Information S1.

The governing equation for PFAS in the thin water films of pore body i yields

$$\begin{aligned}&\frac{\partial\left(V_i s_{w,i}^f c_i^f\right)}{\partial t}+\frac{\partial\left(a_{aw,i}^f K_{aw,i}^f c_i^f\right)}{\partial t}+\frac{\partial\left(a_{sw,i}^f K_{sw,i}^f\left(c_i^f\right)^{N_{sw,i}^f}\right)}{\partial t}\\&+\sum_{j=1}^{n_i}\left(c_{ij}^f q_{w,ij}^f+a_{w,ij}^f D_0^f\frac{c_i^f-c_j^f}{l_{ij}^f}+D_{aw}^f L_{aw,ij}^f\frac{K_{aw,i}^f c_i^f-K_{aw,j}^f c_j^f}{l_{ij}^f}\right)\\&-D_0^f L_{aw,i}^f h_i^f\frac{c_i^b-c_i^f}{l_i^f}-D_{aw}^f L_{aw,i}^f\frac{K_{aw,i}^b c_i^b-K_{aw,i}^f c_i^f}{l_i^f}=0,\end{aligned}\tag{14}$$

where s_i^f is the thin-water-film water saturation, c_{ij}^f is the PFAS concentration in the upstream of the thin-water-film flow, $a_{w,ij}^f$ is the cross-sectional area of thin water films in the pore throat ij (see Figure S1 in Supporting

Information S1), and $K^f_{sw,i}$ and $N^f_{sw,i}$ are the Freundlich isotherm parameters for the solid-phase adsorption at the thin-water-film solid–water interfaces. Note that the surface diffusion flux is zero for water-saturated pore throat.

The air–water interfacial adsorption coefficients $K^b_{aw,i}$ and $K^f_{aw,i}$ in Equations 13 and 14 are a function of the aqueous PFAS concentration, which can be modeled by the Gibbs adsorption equation combined with the Szyzskowski equation as

$$K^b_{aw,i} = \frac{1}{R_g T}\frac{\sigma_0 \beta}{\alpha + c^b_i} \;\&\; K^f_{aw,i} = \frac{1}{R_g T}\frac{\sigma_0 \beta}{\alpha + c^f_i}, \tag{15}$$

where $R_g = 8.314$ J/K/mol is the universal gas constant, T is temperature in Kelvin, α and β are the Szyszskowski fitting parameters that can be determined from measured surface tension data, σ_0 is the surface tension in the absence of PFAS.

For a water-saturated pore body, no thin water films exist. The governing equation for PFAS in thin water films (i.e., Equation 14) is degenerate. In addition, the mass flux between bulk capillary water and thin water films in the governing equation for PFAS in bulk capillary water (i.e., Equation 13) becomes zero.

In a porous medium, only a fraction of the solid surfaces provides adsorption sites for PFAS (e.g., the solid surface of organic carbon or clay minerals). We simplify the solid-phase adsorption in our pore network model by assuming that all of the solid surfaces provide adsorption sites for PFAS. The adsorption capacity of the solid surface in the pore network represents the average adsorption capacity of the porous medium, that is, the adsorption coefficients $K^b_{sw,i}$ and $K^f_{sw,i}$ equal to the solid–water interfacial adsorption coefficient measured in a water-saturated soil sample normalized by its total solid surface area. The assumption of homogeneous solid-phase adsorption allows us to focus on the manifestation of the heterogeneous pore-scale air–water interfacial adsorption in the bulk capillary water and thin water films.

Equations 13 and 14 presented above account for potential mass-transfer limitations between the bulk capillary water and thin water films in each water-unsaturated pore body. For comparison, we formulate a base model that assumes no mass-transfer limitations, that is, $c^f_i = c^b_i$ for all pore bodies. Using c_i to denote the aqueous PFAS concentration in the bulk capillary water and thin water films (if they exist) in pore body i, we obtain the governing equation for PFAS in pore body i as

$$\begin{aligned}\frac{\partial(V_i s_{w,i} c_i)}{\partial t} + \frac{\partial(K_{aw,i} a_{aw,i} c_i)}{\partial t} + \frac{\partial\left(a_{sw,i} K_{sw,i} c_i^{N_{sw,i}}\right)}{\partial t} \\ + \sum_{j=1}^{n_i} \delta_{ij}\left(c_{ij} q^b_{w,ij} + a^b_{w,ij} D^b_0 \frac{c_i - c_j}{l_{ij}} + D^b_{aw} L^b_{aw,ij} \frac{K_{aw,i} c_i - K_{aw,j} c_j}{l_{ij}}\right) \\ + \sum_{j=1}^{n_i}\left(c_{ij} q^f_{w,ij} + D^f_0 a^f_{w,ij} \frac{c_i - c_j}{l^f_{ij}} + D^f_{aw} L^f_{aw,ij} \frac{K_{aw,i} c_i - K_{aw,j} c_j}{l^f_{ij}}\right) = 0,\end{aligned} \tag{16}$$

where $s_{w,i} = s^b_{w,i} + s^f_{w,i}$ is the total water saturation in pore body i, $a_{aw,i} = a^b_{aw,i} + a^f_{aw,i}$ is the total air–water interfacial area, and $a_{sw,i} = a^b_{sw,i} + a^f_{sw,i}$ is the total solid–water interfacial area.

2.4. Numerical Methods

We compute the water saturation and the air–water configuration in each pore body using the percolation algorithm described in Section 2.2. After that, we solve Equation 2 to obtain the water pressure $p_{w,i}$ in each pore body and the bulk capillary water and thin-water film velocity in each pore throat. The air–water configuration and the velocity field are then used to solve the equations for PFAS transport in the pore network. For the complete transport model (i.e., Equations 13 and 14), the primary variables are c^b_i and c^f_i in each pore body i. Conversely, the base model (i.e., Equation 16) only has one primary variable c_i in each pore body i. We solve the equations implicitly (backward Euler) using the Newton-Raphson method.

For the transport simulation, we solve Equations 13 and 14 or Equation 16 using the Newton-Raphson method. We employ an adaptive time step size by cutting or increasing the time step size based on the number of iterations needed for the Newton-Raphson solver to converge. Specifically, if the Newton-Raphson solver does not converge after a maximum number of iterations (set to 10 in our study), we cut the time step size by half and recompute the

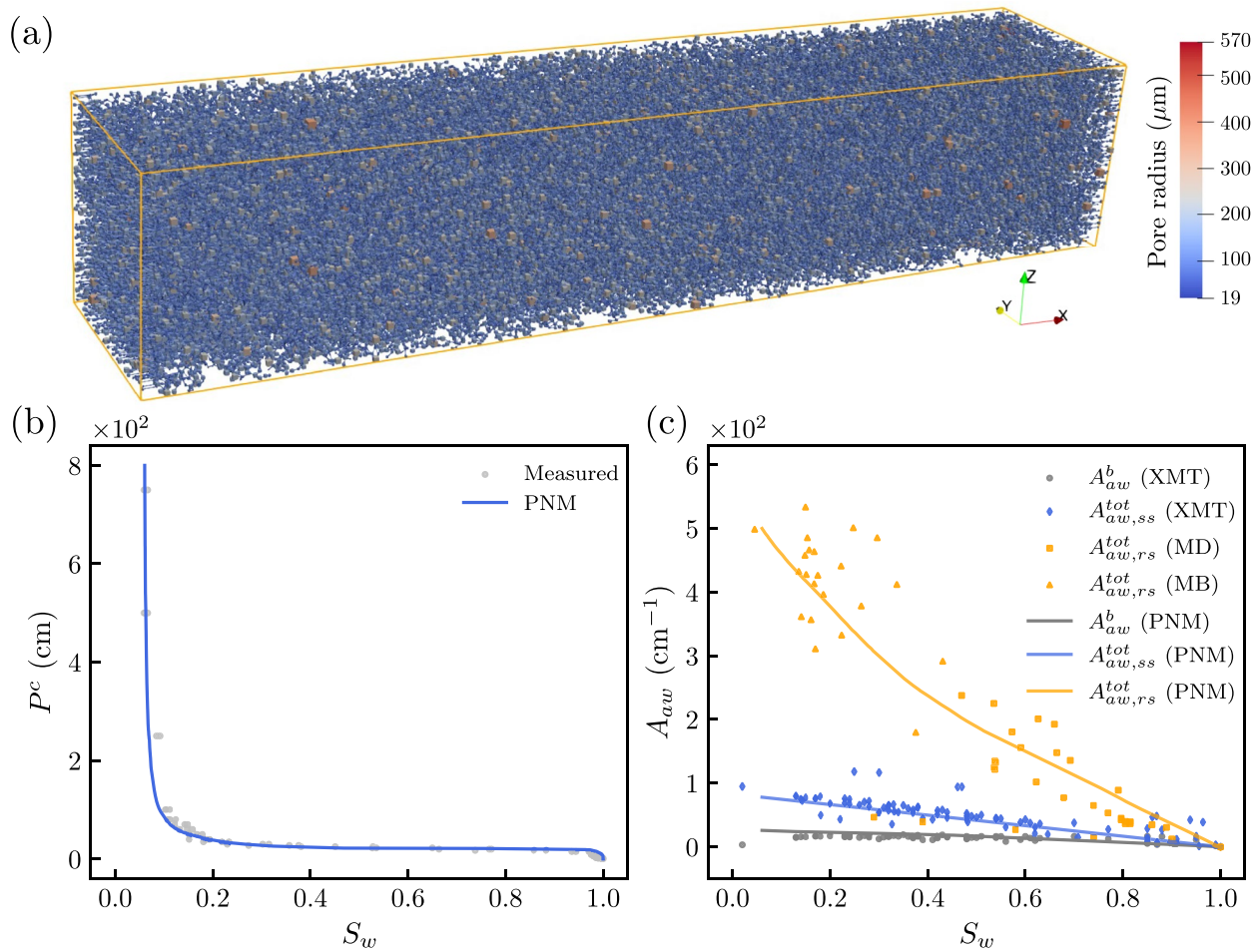

Figure 3. (a) Calibrated pore-network representation of a sand medium, (b) experimentally measured P^c–S_w curve (denoted by "Measured") versus that simulated by the pore-network model (denoted by "PNM"), and (c) experimentally measured A_{aw}–S_w curves versus that simulated by the pore-network model. Panel (c) includes three types of measured A_{aw}: (1) bulk capillary A_{aw} measured by X-ray microtomography (denoted by "A^b_{aw} (XMT)"), (2) total A_{aw} (combining bulk capillary and thin-water-film A_{aw}) assuming smooth grain surfaces measured by X-ray microtomography (denoted by "$A^{tot}_{aw,ss}$ (XMT)"), and (3) total A_{aw} (combining bulk capillary and thin-water-film A_{aw}) measured by aqueous interfacial partitioning tracer test experiments accounting for the impact of microscale surface roughness (denoted by "$A^{tot}_{aw,rs}$"). The $A^{tot}_{aw,rs}$ measured by two types of tracer test experiments are included—miscible displacement experiment (denoted by "$A^{tot}_{aw,rs}$ (MD)") (Brusseau et al., 2007) and mass balance experiment (denoted by "$A^{tot}_{aw,rs}$ (MB)") (Araujo et al., 2015). The three corresponding simulated A_{aw} are denoted by "A^b_{aw} (PNM)", "$A^{tot}_{aw,ss}$ (PNM)", and "$A^{tot}_{aw,rs}$ (PNM)", respectively.

current time step. If the Newton-Raphson solver converges fewer than half of the maximum number of iterations, we double the time step size and move to the next time step. For situations other than these two, the time step size remains unchanged. We also set a maximum time step size to prevent unrealistically large time step sizes. The initial and maximum time step sizes are set to 1/100 and 1/10 of the residence time of water in the pore network, respectively. The convergence tolerance (i.e., the L_∞ of the update of primary variables—PFAS concentrations) for the Newton-Raphson iterations is set to 10^{-12} mg/L.

3. Pore-Network Modeling of PFAS Transport in a Water-Unsaturated Sand Medium

We apply the pore-network modeling framework (Section 2) to simulate PFAS transport in an example sand medium under water-unsaturated conditions. Below, we present details about the construction of the pore network and the design of the numerical experiments.

3.1. Pore-Network Representation of a Well-Characterized Sand Medium

We construct an unstructured pore network that consists of 30 × 30 × 150 randomly distributed pore bodies (see Figure 3a) to represent the pore structure of a commercially available 45/50 mesh quartz sand (UNIMIN Corp.)

whose grain size (diameter d) distribution is: 250 μm ≤ d < 300 μm (1.4%), 300 μm ≤ d < 355 μm (47.1%), 355 μm ≤ d < 425 μm (51.4%), and d ≥ 425 μm (0.1%). The sand medium is experimentally well-characterized. The detailed characterization data, including porosity, mean grain size, grain size uniformity, geometrical smooth solid surface area, and actual rough solid surface area, are reported in the literature including Peng and Brusseau (2005); Brusseau et al. (2007); Jiang et al. (2020b). The capillary pressure water saturation curve (P^c–S_w) and the specific air–water interfacial area curve (A_{aw}–S_w) measured by various methods were reported in the literature (Araujo & Brusseau, 2020; Araujo et al., 2015; Brusseau et al., 2007). Note that A_{aw} denotes the *specific* air–water interfacial area in the pore network, which is different from a_{aw} (i.e., the air–water interfacial area in a pore body) in Section 2. These experimental data are used to constrain the pore-network structures, including the distributions of pore body and pore throat sizes, the coordination number, and the surface roughness. The specifics are presented below.

We begin by using the measured P^c–S_w curve to calibrate the distributions of pore body and pore throat sizes, and pore body connectivity (i.e., coordination number). The calibration process is as follows: Step 1—Construct an unstructured pore network using an initial pore body size distribution (assuming lognormal distributions) obtained by fitting a bundle-of-tubes model to the measured P^c–S_w curve; Step 2—Determine the size of each pore throat ij by multiplying the minimum size of its connected pore bodies i and j by a ratio (namely, pore body-to-throat size aspect ratio); Step 3—Apply the percolation algorithm to the pore network to compute its P^c–S_w curve and compare it with the measured P^c–S_w curve from Brusseau et al. (2007); Step 4—Repeat steps 1–3 until a good agreement between the simulated and measured P^c–S_w curves is obtained. During the above processes, we tune the mean pore size, pore size standard deviation, pore body-to-throat size aspect ratio, and pore connectivity when repeating step 1, and randomly shrink a small fraction of pore throats when repeating step 2. Figure 3b shows the final comparison between the simulated and measured P^c–S_w curves. The mean and standard deviation of pore body sizes are 106.4 and 40.7 μm, the mean and standard deviation of pore throat sizes are 65.8 and 37.3 μm, and the mean coordination number is 3.2. The pore body and pore throat size distributions are presented in Figure S2 in Supporting Information S1.

Then, we validate the pore-network representation calibrated from the measured P^c–S_w curve by simulating the A_{aw} measured by X-ray microtomography (XMT). The measured A_{aw} includes the area of bulk capillary air–water interfaces $\left(A_{aw}^{b}\right)$ and the total area of bulk capillary and thin-water-film air–water interfaces $\left(A_{aw}^{tot}\right)$. Because the XMT images do not resolve the microscale surface roughness, the total air–water interfacial area measured by XMT represents the air–water interfacial area that assumes smooth grain surfaces (Araujo & Brusseau, 2020). We denote the XMT-measured total air–water interfacial area as $A_{aw,ss}^{tot}$—the subscript "ss" represents smooth surface. Comparing with the XMT air–water interfacial areas allows us to validate the pore-network representation independent of the grain surface roughness. Figure 3c shows an excellent agreement between the predicted and XMT-measured A_{aw}^{b} and $A_{aw,ss}^{tot}$ over a wide range of water saturation degrees, which provides a direct validation of the pore-network representation calibrated from the measured P^c–S_w curve.

Finally, we calibrate the surface roughness parameters (i.e., X, k, and h_m) by comparing the simulated A_{aw} with that measured by aqueous-phase interfacial partitioning tracers. The A_{aw} measured by aqueous-phase interfacial partitioning tracers represents the total area of bulk capillary and thin-water-film air–water interfaces, which accounts for the impact of grain surface roughness. The air–water interfacial areas were measured by either miscible displacement experiments (Brusseau et al., 2007) or mass balance experiments that were based on mass partitioning of the aqueous-phase interfacial partitioning tracer in an unsaturated medium assuming chemical equilibrium conditions (Araujo et al., 2015). We denote the air–water interfacial area measured by aqueous-phase interfacial partitioning tracers as $A_{aw,rs}^{tot}$—the subscript "rs" represents rough surface. After calibration, X = 9.2, k = 0.42, and h_m = 13.9 nm give a good agreement between the simulated and measured $A_{aw,rs}^{tot}$ (see Figure 3c).

In the final pore network, the simulated water and air–water interfacial areas are distributed relatively uniformly across the lateral direction of the pore network at different pore-network-averaged water saturations (see Figure S3 in Supporting Information S1), which suggests that the pore network is sufficiently large for flow and transport analysis at a representative-elementary-volume scale. The cross-section-averaged water saturation and air–water interfacial area at two pore-network-averaged water saturation values (i.e., S_w = 0.5 and S_w = 0.3) are presented in Figure S4 in Supporting Information S1.

3.2. Design of the Pore-Network Modeling Experiments

We conduct four sets of numerical experiments in the pore network to study the transport of PFAS under water-unsaturated conditions. The first set includes three simulations: (a) not accounting for PFAS adsorption at air–water and solid–water interfaces (i.e., nonreactive tracers), (b) only accounting for PFAS adsorption at bulk

Table 1
Design of the Four Simulation Sets Used in the Numerical Experiments

Simulation sets	Bulk capillary SWIA and AWIA[a]	Thin water-film SWIA and AWIA	Intra-pore mass-transfer limitations	SD[b]	DPR[c]
#1	×	×	×	×	×
	✓	×	×	×	×
	✓	✓	×	×	×
#2	✓	✓	×	×	×
	✓	✓	✓	×	×
#3	✓	✓	×	✓	×
	✓	✓	✓	✓	×
#4	✓	✓	×	✓	✓
	✓	✓	✓	✓	✓

[a]SWIA and AWIA refer to solid–water and air–water interfacial adsorption, respectively. [b]SD refers to surface diffusion. [c]DPR refers to discontinuous pendular rings.

capillary air–water and solid–water interfaces, and (c) accounting for PFAS adsorption at bulk capillary and thin-water-film air–water and solid–water interfaces. The first set of simulations are considered as the base simulations. They do not account for surface diffusion of PFAS adsorbed at air–water interfaces, mass-transfer limitations between bulk capillary water and thin water films inside each water-unsaturated pore body (referred to as *intra-pore mass-transfer limitations* hereafter), or the disconnect of bulk capillary water under drier conditions. These three factors are examined by the other three simulation sets. See detailed designs for all of the four simulation sets in Table 1. Note that when the bulk capillary water disconnects in some pore bodies, water in those pore bodies is only connected by thin water films, which introduces additional mass-transfer limitations in those pore clusters. The disconnect of bulk capillary water is accounted for in the fourth simulation set (using the algorithm presented in Section 2.2.1).

To examine the dependence of air–water interfacial adsorption and mass-transfer limitations on wetting condition, surface roughness, and PFAS chain length, all simulations in Table 1 consider two averaged water saturation values in the pore network (i.e., $S_w = 0.5$ and $S_w = 0.3$), two representations of surface roughness (i.e., smooth and rough surfaces), and three PFAS (i.e., a shorter-chain PFAS presented by PFPeA, and two longer-chain PFAS represented by PFOA and PFOS). For each simulation, we impose a unit pressure gradient across the pore network to establish a steady-state water flow field that effectively represents gravity-driven flow. Then, we inject 10 pore volumes of PFAS solution at the inlet at the concentration of 1 mg/L, which is representative of pore water concentration measured in some PFAS source zones (Anderson et al., 2022; Quinnan et al., 2021; Schaefer et al., 2022). A zero gradient of aqueous PFAS concentration is applied at the outlet of the pore network. The parameters for PFAS transport and adsorption are presented in Table 2.

4. Results and Analysis

4.1. Contribution of Thin-Water-Film Air–Water Interfaces to PFAS Retention

We use the first simulation set to examine the contribution of the thin-water-film air–water interfaces to PFAS retention. These simulations neglect surface diffusion of PFAS adsorbed at air–water interfaces, intra-pore mass-transfer limitations between bulk capillary water and thin water films inside each water-unsaturated pore body, and the disconnect of bulk capillary water under drier conditions as explained in Section 3.2. Because the sand medium employed in our simulations has negligible solid-phase adsorption capacity for all three PFAS, our analysis in this and the following sections focus on the adsorption at air–water interfaces only. In each simulation, we model the breakthrough curves and compute the retardation factors by analyzing the temporal moments. The breakthrough curve represents the temporal evolution of the average aqueous PFAS concentration at the

Table 2
Transport and Adsorption Parameters for PFAS Including Molecular Weight, Aqueous Diffusion Coefficient (Schaefer, Drennan, et al., 2019), Surface Diffusion Coefficient (Karakashev & Ivanova, 2010; Stoyanov & Denkov, 2001; Valkovska & Danov, 2000, 2001), and Coefficients for Adsorption at Air–Water Interfaces and Solid–Water Interfaces (Brusseau, 2020; Brusseau & Van Glubt, 2019; Guo et al., 2020; Van Glubt et al., 2021)

Parameters	Units	PFPeA	PFOA	PFOS
Molecular weight	g/mol	264.046	414.07	500.13
D_0^b, D_{aw}^b, D_0^f, D_{aw}^f	cm^2/s	1.2e−5	4.9e−6	5.4e−6
α	$\mu mol/cm^3$	6.82	5.97e−2	8.2e−3
β	–	0.132	0.120	0.118
K_{sw}^b, K_{sw}^f	$cm \cdot (\mu mol/cm^3)^{1-N_{sw}}$	2.92e−6	1.23e−5	8.33e−6
N_{sw}^b, N_{sw}^f	–	0.87	0.87	0.81

Note. A few other parameters are not presented in the table, which include $A_{svl} = 6 \times 10^{-20}$ J (Or & Tuller, 1999), $T = 293.15$ K, and $\sigma_0 = 71$ dyn/cm.

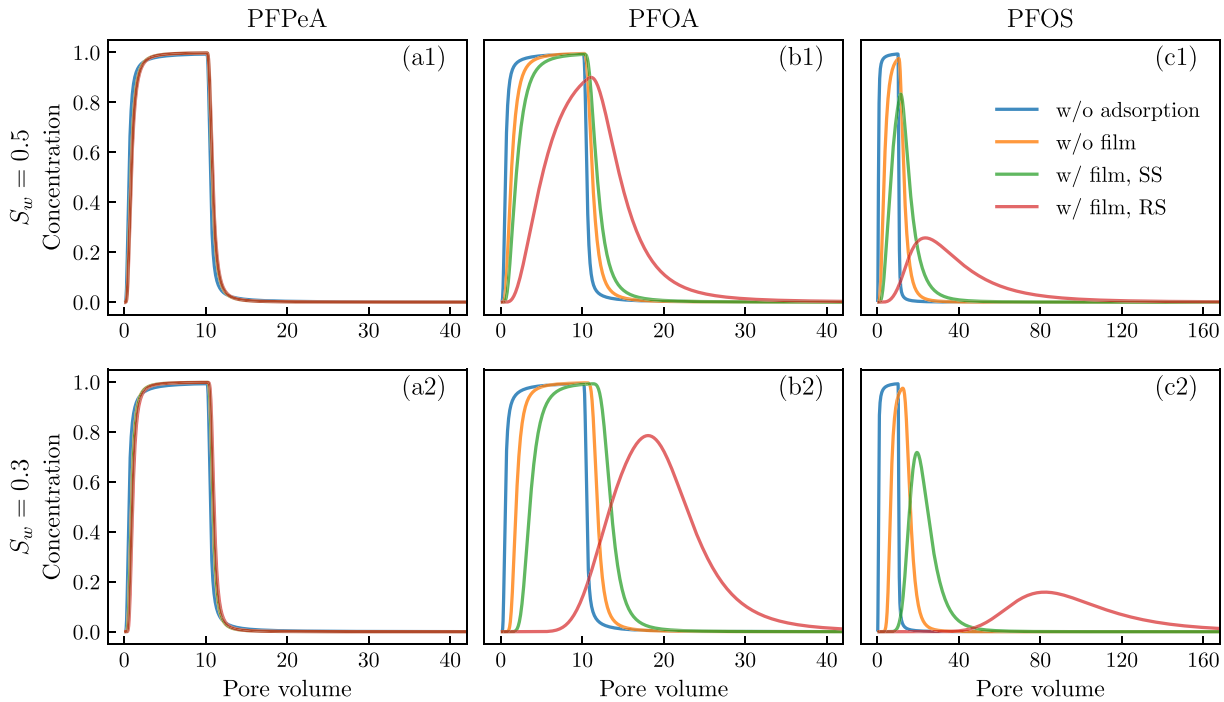

Figure 4. Simulated breakthrough curves by the pore-network model for three PFAS (i.e., PFPeA, PFOA, and PFOS), two pore-network-averaged water saturation S_w (i.e., $S_w = 0.5$ and $S_w = 0.3$), and with and without accounting for grain surface roughness (smooth surface is denoted by "SS" and rough surface is denoted by "RS"). For each scenario, three cases are simulated: no adsorption of PFAS at air–water and solid–water interfaces (denoted by "w/o adsorption"), adsorption of PFAS at bulk capillary air–water interfaces and solid–water interfaces but not accounting for the presence of thin water films (denoted by "w/o film"), and adsorption of PFAS at both bulk capillary and thin-water-film air–water interfaces and solid–water interfaces (denoted by "w/ film"). All simulations assume chemical equilibrium between bulk capillary water and thin water films inside each water-unsaturated pore body, and do not account for surface diffusion of PFAS adsorbed at air–water interfaces, and the disconnect of bulk capillary water (i.e., assuming continuous pendular rings).

outlet of the pore network normalized by the injection concentration at the inlet. The retardation factor reflects the degree of PFAS retention. Here the retardation factor is given by $R = \mu_1^{\text{inlet}} - \mu_1^{\text{outlet}}$, where μ_1^{inlet} and μ_1^{outlet} are respectively the first temporal central moments of the average aqueous concentration at the inlet and outlet and $\mu_1 = \int_0^\infty tC(t)dt / \int_0^\infty C(t)dt$ with t being the dimensionless time and $C(t)$ being the aqueous concentration normalized by the injection concentration at the inlet.

As shown in Figures 4a1 and 4a2, due to relatively weak adsorption at air–water interfaces, the breakthrough curves of shorter-chain PFAS (i.e., PFPeA whose K_{aw} is 5.7×10^{-5} cm as shown in Table S1 of Supporting Information S1) almost overlap regardless of the existence of thin water films. Correspondingly, the retardation factors are almost identical (see Table S2 in Supporting Information S1).

However, the breakthrough curves of longer-chain PFAS (i.e., PFOA and PFOS) suggest significant retention behaviors when thin water films are included (see Panels b1, b2, c1, and c2 in Figure 4). The computed retardation factors for PFOA and PFOS, when thin water films are included, are 1.4∼9.0 times (for $S_w = 0.5$) and 3.9∼13 times (for $S_w = 0.3$) greater than those without the presence of thin water films (see Table S2 in Supporting Information S1). This contrast indicates that the adsorption at the thin-water-film air–water interfaces contributes significantly to the overall retention of longer-chain PFAS in the pore network even at relatively high water saturations for the sand medium used in the present study.

Additionally, the relative importance of adsorption at thin-water-film air–water interfaces depends on several other factors, including surface roughness and water saturation (or capillary pressure). For the sand medium used in our simulations, the presence of surface roughness increases the retardation factors by 2.7∼5.2 times (see Table S2 in Supporting Information S1). The retention also increases as the water saturation decreases. The retardation factors for $S_w = 0.3$ are 1.7∼2.6 times greater than that of $S_w = 0.5$ (see Table S2 in Supporting Information S1). The greater retention at a lower water saturation is due to the increased air–water interfacial area from the newly formed thin water films on the pore walls. These observations are consistent with how the relative contributions of thin-water-film and bulk capillary air–water interfaces change with water saturation in the sand medium (see Figure 3).

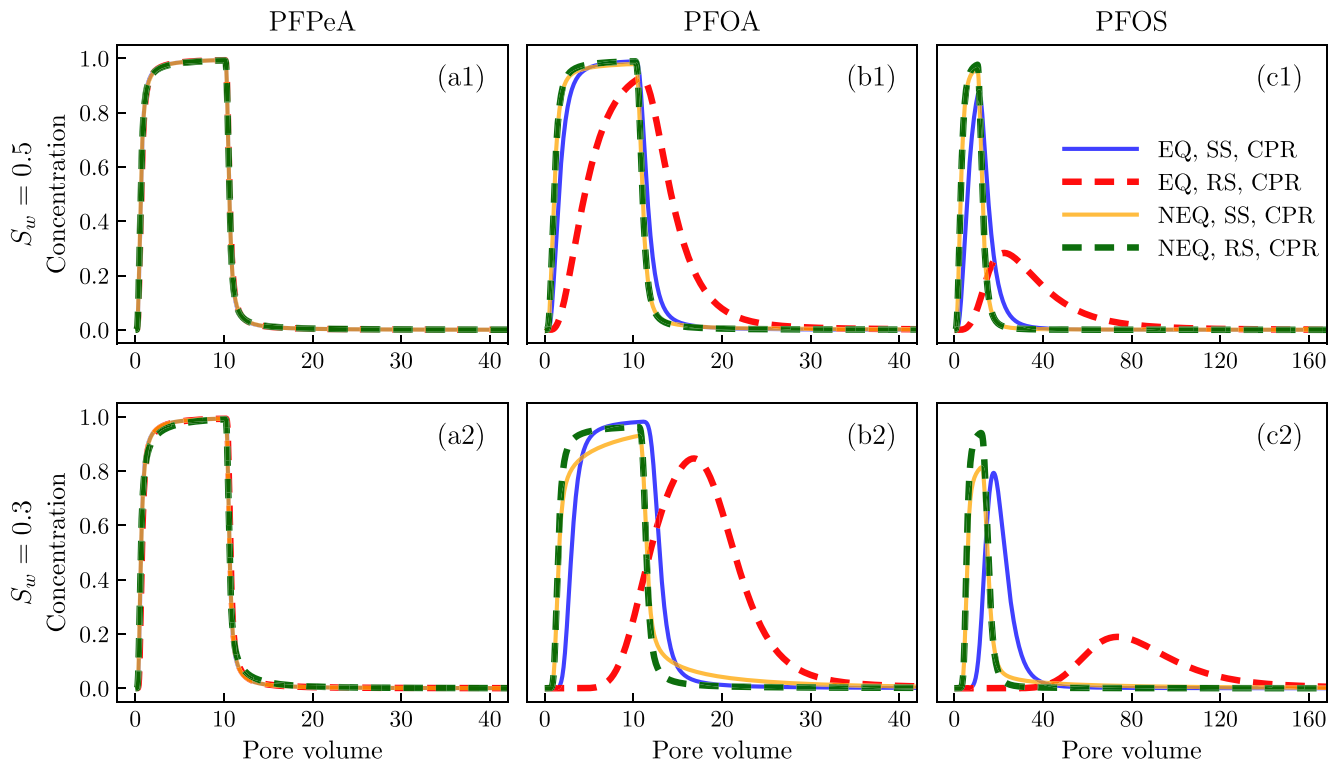

Figure 5. Simulated breakthrough curves by the pore-network model for three PFAS (i.e., PFPeA, PFOA, and PFOS), two pore-network-averaged water saturation S_w (i.e., $S_w = 0.5$ and $S_w = 0.3$), and with and without accounting for grain surface roughness (smooth surface is denoted by "SS" and rough surface is denoted by "RS"). For each scenario, two cases are simulated: assuming chemical equilibrium between bulk capillary water and thin water films inside each water-unsaturated pore body (denoted by "EQ"), and accounting for intra-pore mass-transfer limitations between bulk capillary water and thin water films inside each water-unsaturated pore body (denoted by "NEQ"). All simulations do not account for the surface diffusion of PFAS adsorbed at air–water interfaces and the disconnect of bulk capillary water (i.e., assuming continuous pendular rings, denoted by "CPR").

4.2. Impact of Thin-Water-Film Mass-Transfer Limitations on PFAS Transport

4.2.1. Continuous Pendular Rings

The second and third simulation sets assume all bulk capillary water in the pore network is well connected (i.e., assuming continuous pendular rings in the sand medium), which allows us to focus on examining how intra-pore mass-transfer limitations between bulk capillary water and thin water films inside each water-unsaturated pore body influence the PFAS transport. To evaluate the importance of surface diffusion of PFAS adsorbed at air–water interfaces, we analyze the impact of intra-pore mass-transfer limitations without (the second simulation set) and with (the third simulation set) accounting for surface diffusion. The dependence of intra-pore mass-transfer limitations and surface diffusion on various factors—PFAS chain length, surface roughness, and water saturation—are also discussed.

The second simulation set (surface diffusion not included) shows that intra-pore mass-transfer limitations lead to significant deviation in the breakthrough curves for PFOA and PFOS from those in the base simulations that exclude intra-pore mass transfer limitations (i.e., assuming chemical equilibrium between bulk capillary water and thin water films inside each water-unsaturated pore body) (see Figure 5). However, this is not the case for PFPeA. A closer inspection reveals that the adsorbed mass of PFPeA at the thin-water-film air–water interfaces is negligible—it accounts for less than 4.7%∼11% (see Figure 6). While intra-pore mass-transfer limitations are still present, the amount of PFPeA mass that the thin water films can hold is minor and thus the mass-transfer limitations have almost no impact on the overall transport of PFPeA in the pore network. Because of the negligible impact of mass-transfer limitations for PFPeA, we focus on analyzing the two more interfacially active longer-chain PFAS in the rest of the paper. In contrast, the adsorbed mass of PFOA and PFOS at the thin-water-film air–water interfaces is much greater than those in the bulk capillary water and bulk capillary air–water interfaces—it accounts for 75%∼84% for PFOA and 88%∼91% for PFOS (see Figure 6). Because the thin water

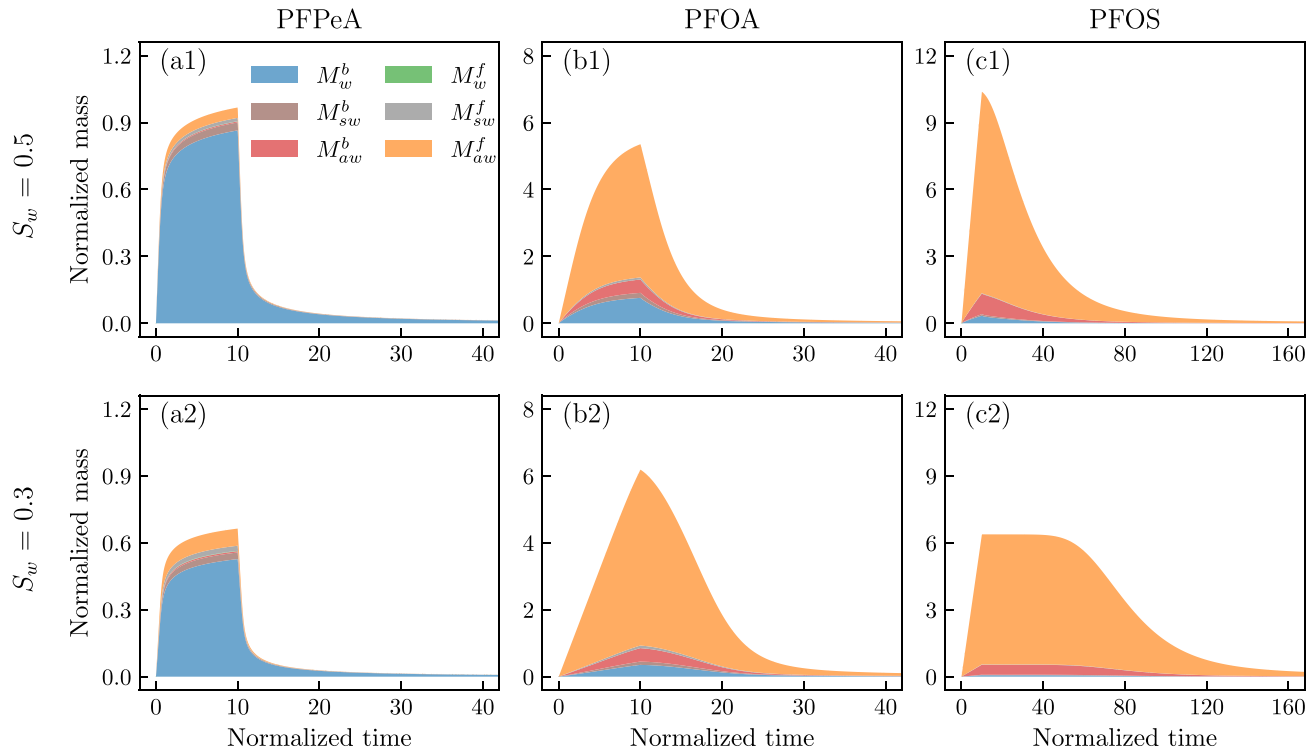

Figure 6. The fractions of PFAS mass in the bulk water (M_w^b, aqueous), bulk capillary solid–water interfaces (M_{sw}^b, solid-phase adsorption), bulk capillary air–water interfaces (M_{aw}^b, air–water interfacial adsorption), thin water films (M_w^f, aqueous), thin-water-film solid–water interfaces (M_{sw}^f, solid-phase adsorption), thin-water-film air–water interfaces (M_{aw}^f, air–water interfacial adsorption). All simulations account for PFAS adsorption at air–water and solid–water interfaces and grain surface roughness, but they all assume chemical equilibrium between bulk capillary water and thin water films inside each water-unsaturated pore body, and do not account for surface diffusion of PFAS adsorbed at air–water interfaces, and the disconnect of bulk capillary water (i.e., assuming continuous pendular rings).

films can hold a significant amount of mass for these more interfacially active PFAS, mass-transfer limitations between the bulk capillary water and thin water films strongly influence the overall transport of PFOA and PFOS. Comparing PFOA and PFOS, the latter is more interfacially active and hence is expected to be more strongly influenced by the intra-pore mass-transfer limitations. This is consistent with our observations in Figure 5.

The deviation of the breakthrough curves from the base cases represents the nonequilibrium behaviors caused by the intra-pore mass-transfer limitations. The extent of nonequilibrium behaviors can be quantified by computing the relative difference between the second central moments of the breakthrough curves (Valocchi, 1985, 1990), $\epsilon_{\mu_2} = |\mu_{2,EQ} - \mu_{2,NEQ}|/\mu_{2,EQ}$, where $\mu_{2,EQ}$ and $\mu_{2,NEQ}$ are the second central moments for simulations without and with accounting for intra-pore mass-transfer limitations, respectively. The second central moment is given by $\mu_2 = \int_0^\infty (t-\mu_1)^2 C(t)dt / \int_0^\infty C(t)dt$, where μ_1 is the first central moment as defined and computed in Section 4.1. As expected, ϵ_{μ_2} increase with the interfacial activity of PFAS (PFOS > PFOA > PFPeA)—ϵ_{μ_2} are up to 2.8% for PFPeA, 38% for PFOA, and 79% for PFOS.

We can also use the second central moment to quantify how the surface roughness and water saturation influence the nonequilibrium behaviors in the breakthrough curves. In the presence of surface roughness, ϵ_{μ_2} increases by 1.3∼4.7 times for PFPeA, 1.04∼2.5 for PFOA, and 1.2∼12 for PFOS (see Table 3), which indicates that surface roughness strongly enhances the nonequilibrium behaviors. Microscale roughness on soil grains increases the length of thin water films, which subsequently increases the time scale of intra-pore mass transfer between the bulk capillary water and thin water films inside each water-unsaturated pore body. This can be shown by analyzing the Damköhler number (see details in Section S1 and Table S4 in Supporting Information S1). As expected, the presence of surface roughness reduces the Damköhler number by 49∼57 times. Because the pore water velocity (v_p) remains almost unchanged, the reduced Damköhler number and hence the more significant nonequilibrium behaviors can be entirely attributed to the greater intra-pore mass-transfer time scale in the presence of surface roughness. For the different water saturations, we observe that the computed ϵ_{μ_2} for $S_w = 0.3$ is 2.5∼25 times smaller than that for $S_w = 0.5$ (see Table 3). A closer inspection reveals that the pore water velocity v_p at $S_w = 0.3$

Table 3
Difference Between the Second Central Moments (μ_2) for Simulations Without and With Accounting for the Intra-Pore Mass-Transfer Limitations Between Bulk Capillary Water and Thin Water Films Inside Each Water-Unsaturated Pore Body (i.e., $\epsilon_{\mu_2} = |\mu_{2,NEQ} - \mu_{2,EQ}|/\mu_{2,EQ}$)

Surface diffusion	S_w	PFPeA		PFOA		PFOS	
		Smooth	Rough	Smooth	Rough	Smooth	Rough
×	0.5	3.6e−3	1.7e−2	1.5e−1	3.8e−1	6.4e−1	7.9e−1
	0.3	2.2e−2	2.8e−2	5.0e−2	5.2e−2	2.6e−2	3.2e−1
✓	0.5	3.7e−3	4.3e−3	4.1e−3	1.9e−2	6.8e−3	1.3e−2
	0.3	5.5e−3	8.3e−3	1.9e−3	3.6e−3	1.4e−3	1.6e−3

Note. All simulations do not account for the disconnect of bulk capillary water (i.e., assuming continuous pendular rings).

is 3.6 times smaller. Correspondingly, the Damköhler number increases by 7.2∼8.4 times (see Table S4 in Supporting Information S1). This suggests that the nonequilibrium behaviors become less significant under a drier condition when both surface diffusion and the disconnect of bulk capillary water are not accounted for.

A direct indicator of the nonequilibrium behaviors is the early arrival and long tailing in the breakthrough curves. We define the arrival time as the time when 0.1% of the total injected PFAS mass reaches the outlet, and define the depletion time as the time when 99.9% of the injected PFAS mass is recovered at the outlet. When the intra-pore mass-transfer limitations are included, the arrival time is 1.3∼5.9 times smaller for PFOA and 1.7∼9.4 times smaller for PFOS. Similarly, the depletion time is up to 10 times greater for PFOA and 5.2 times greater for PFOS.

Up to now, all the presented results are from the second simulation set, which neglects an important transport process—surface diffusion of PFAS adsorbed along the air–water interfaces. As discussed in the *Introduction*, surface diffusion may substantially accelerate the intra-pore mass transfer between the bulk capillary water and thin water films inside each water-unsaturated pore body, and hence reduce intra-pore mass-transfer limitations. We now analyze the third simulation set (surface diffusion included) to quantify the impact of surface diffusion on the intra-pore mass-transfer limitations and the resulting nonequilibrium behaviors in the breakthrough curves. Unlike the results from the second simulation set that does not include surface diffusion, accounting for surface diffusion completely eliminates the nonequilibrium behaviors in the breakthrough curves (see Figure 7). The simulated breakthrough curves without and with representing the intra-pore mass-transfer limitations are identical, regardless of PFAS chain length, surface roughness, and S_w. This is also confirmed by the several orders of magnitude lower ϵ_{μ_2} (see Table 3). Further analysis reveals that surface diffusion has increased the mass-transfer rate between the thin water film and bulk capillary water by 542 609 times for PFOA and $3.2 \times 10^3 \sim 4.4 \times 10^3$ times for PFOS. The orders of magnitude greater mass-transfer rates suggest that surface diffusion of PFAS at air–water interfaces is the most important process responsible for the mass transfer between bulk capillary water and thin water films. Because of surface diffusion, PFAS in the bulk capillary water and thin water films inside the water-unsaturated pore bodies can be assumed in chemical equilibrium.

4.2.2. Discontinuous Pendular Rings

The second and third simulation sets discussed above assume that all of the pendular rings in the soil medium is connected. However, this assumption may be invalid under drier conditions when the pendular rings between soil grains disconnect from each other. As pendular rings disconnect between some pores, their hydraulic connectivity is only provided by thin water films. The fourth simulation set relaxes this critical assumption by explicitly representing the disconnect of bulk capillary water in the pore network under drier conditions. The disconnect of bulk capillary water in large clusters of pores is expected to greatly increase the time scale of mass transfer in the pore network, which could subsequently enhance the nonequilibrium behaviors of PFAS transport. This subsection focuses on examining this issue.

In contrast to the simulations that assume continuous pendular rings (Section 4.2.1), accounting for the disconnect of bulk capillary water leads to strong nonequilibrium behaviors in the breakthrough curves even in the presence of surface diffusion (see Figure 7). The computed ϵ_{μ_2} range from 21%∼150% for PFOA and 81%∼240% for PFOS (see Table 4). Because surface diffusion removes any intra-pore mass-transfer limitations between the bulk capillary water and thin water films inside each water-unsaturated pore body (see Section 4.2.1 and Figure S5 in Supporting Information S1), the nonequilibrium behaviors observed here can be attributed entirely to the disconnect of bulk capillary water. For the pore bodies whose bulk capillary water is disconnected, mass transfer between them can only occur through the thin water films. As discussed earlier in Section 4.2.1, surface roughness and smaller water saturation both increase the lengths of thin water films and subsequently lead to greater time scales of mass transfer between bulk capillary water and thin water films. When the disconnect of bulk capillary water is accounted for, the reduction in water saturation increases mass transfer limitations by two means. First, it increases the lengths of thin water films inside water-unsaturated pore bodies (see Figure 2). Second, as the water saturation in a soil medium decreases, the clusters of pore bodies with disconnected bulk capillary water increase and subsequently increase the

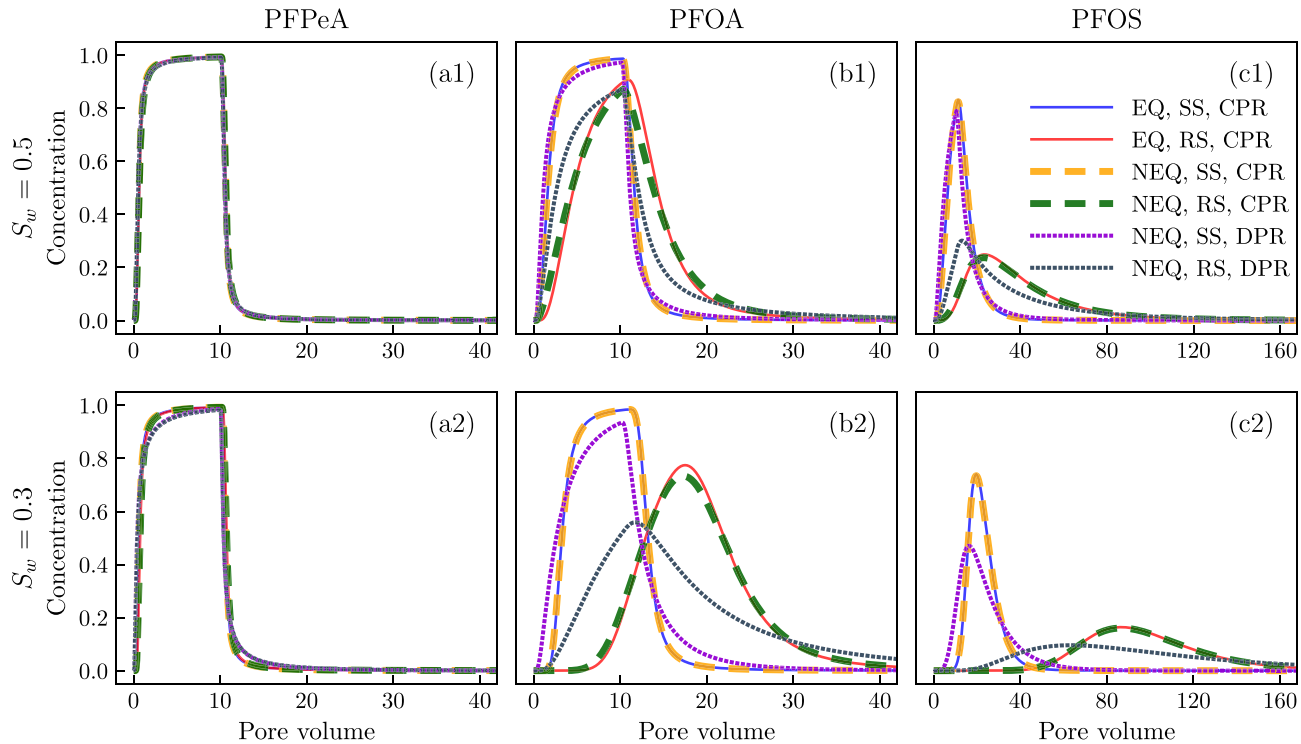

Figure 7. Simulated breakthrough curves by the pore-network model for three PFAS (i.e., PFPeA, PFOA, and PFOS), two pore-network-averaged water saturation S_w (i.e., $S_w = 0.5$ and $S_w = 0.3$), and with and without accounting for grain surface roughness (smooth surface is denoted by "SS" and rough surface is denoted by "RS"). For each scenario, three cases are simulated: assuming chemical equilibrium between bulk capillary water and thin water films inside each water-unsaturated pore body (denoted by "EQ") and continuous pendular rings (denoted by "CPR"), accounting for intra-pore mass-transfer limitations between bulk capillary water and thin water films inside each water-unsaturated pore body (denoted by "NEQ") but not the disconnect of bulk capillary water (i.e., assuming continuous pendular rings, denoted by "CPR"), and accounting for intra-pore mass-transfer limitations between bulk capillary water and thin water films inside each water-unsaturated pore body (denoted by "NEQ") and the disconnect of bulk capillary water (i.e., considering discontinuous pendular rings, denoted by "DPR"). All simulations account for surface diffusion of PFAS adsorbed at air–water interfaces.

overall time scale of mass transfer in the soil medium. To demonstrate that, we recompute the Damköhler number (see details in Section S1 in Supporting Information S1). As shown in Table S4 in Supporting Information S1, the Damköhler numbers for PFOA and PFOS simulations are reduced by 11∼18 times in the presence of disconnected pendular rings, which indicates more strong nonequilibrium behaviors. These results and analyses clearly suggest that the disconnect of bulk capillary water as the water saturation in a soil medium decreases is a primary factor controlling PFAS transport in unsaturated soil media and needs to be represented in mathematical models and data analyses.

Table 4
Difference Between the Second Central Moments (μ_2) for Simulations Not Accounting for the Disconnect of Bulk Capillary Water (i.e., Assuming Continuous Pendular Rings, Denoted by "CPR") and Those Accounting for the Disconnect of Bulk Capillary Water (i.e., Considering Discontinuous Pendular Rings, Denoted by "DPR"), That Is, $\epsilon_{\mu_2} = |\mu_{2,DPR} - \mu_{2,CPR}|/\mu_{2,CPR}$

	PFPeA		PFOA		PFOS	
S_w	Smooth	Rough	Smooth	Rough	Smooth	Rough
0.5	9.3e−2	1.3e−1	2.1e−1	1.3	8.1e−1	1.4
0.3	5.0e−1	4.1e−1	3.4e−1	1.5	8.2e−1	2.4

Note. All simulations account for intra-pore mass-transfer limitations between bulk capillary water and thin water films inside each water-unsaturated pore body, and surface diffusion of PFAS adsorbed at air–water interfaces.

4.3. Impact of Thin-Water-Film Mass-Transfer Limitations on the Accessibility of Thin-Water-Film Air–Water Interfaces

A critical question is whether the mass-transfer limitations in the thin water films reduce the accessibility of thin-water-film air–water interfaces by PFAS. We examine this question by further analyzing the numerical simulations in Section 4.2. The amount of air–water interfacial area accessed by PFAS is reflected in the overall retention they experience moving through the pore network. Thus, the accessed air–water interfacial areas can be estimated from the breakthrough curves at the outlet. To differentiate from the actual A_{aw} in the pore network, we refer to the air–water interfacial area accessed by PFAS as *effective* A_{aw}.

To compute the effective A_{aw}, we first obtain the retardation factors R from the temporal moment analysis presented in Section 4.1. The computed R are then used to estimate the effective A_{aw} via

Table 5
Effective Air–Water Interfacial Areas Computed From the Breakthrough Curves Versus the Actual Air–Water Interfacial Areas in the Pore Network Without (Denoted by "$A_{aw,ss}$") and With (Denoted by "$A_{aw,rs}$") the Presence of Microscale Surface Roughness

				$A_{aw,ss}$ (cm^{-1})			$A_{aw,rs}$ (cm^{-1})		
Concentration	S_w	SD[a]	DPR[b]	PFOA	PFOS	PNM[c]	PFOA	PFOS	PNM
1 mg/L	0.5	×	×	48.9/50.4[d]	45.1/46.2	41.4	184/78.0	200/20.8	189
		✓	×	48.8/48.7	46.0/46.0		188/189	217/217	
		✓	✓	49.4/49.4	47.0/47.0		190/190	218/218	
	0.3	×	×	64.8/66.2	63.3/67.8	57.7	294/247	324/61.7	298
		✓	×	64.4/64.5	62.9/62.9		297/297	345/346	
		✓	✓	64.9/64.8	65.6/65.5		300/300	352/352	
1 μg/L	0.5	×	×	41.3/41.8	39.1/38.7	41.4	185/72.8	181/33.1	189
		✓	×	40.8/40.8	40.7/40.7		186/186	186/186	
		✓	✓	41.0/41.1	40.7/40.7		188/188	192/193	
	0.3	×	×	56.7/56.8	57.9/39.8	57.7	290/233	277/19.2	298
		✓	×	56.5/56.5	56.5/56.5		292/292	292/292	
		✓	✓	56.5/56.3	56.5/56.5		292/292	293/293	

[a]SD refers to surface diffusion. [b]DPR refers to discontinuous pendular rings. [c]PNM refers to the pore-network model. [d]We present the A_{aw} for simulations without (left) and with (right) accounting for intra-pore mass-transfer limitations between bulk capillary water and thin water films inside each water-unsaturated pore body.

$$A_{aw} = \left(\theta(R - R_0) - K_{sw}A_{sw}C^{N-1}\right)/K_{aw}(C), \tag{17}$$

where R_0 is the retardation factor for a nonreactive tracer, θ is the average water content of the pore network, C is a representative concentration (which is assumed equal to the concentration applied at the inlet), A_{sw} is the specific solid–water interfacial area. The other parameters are defined in Section 2 or given in Table 2. We compute the retardation factors and effective A_{aw} for all three simulation sets presented in Section 4.2 (see Table S3 in Supporting Information S1 and Table 5). For the moment analysis, we simulate 5,000 pore volumes of injection and use the full breakthrough curve to compute the retardation factor. We found that not capturing the full breakthrough curve will underestimate the retardation factor due to missing the long tailing of the breakthrough curve, especially for the cases with strong nonequilibrium behaviors. The computed retardation factors and effective A_{aw} become almost identical for all simulations (the relative difference is less than 5% except for the simulations not accounting for surface diffusion but with surface roughness included). The small difference in retardation factors and effective A_{aw} suggests that all thin-water-film air–water interfaces in the pore network are accessed by PFAS in those simulations.

It is interesting that the computed effective A_{aw} are greater than the total actual A_{aw} in the pore network. We hypothesize that the deviation is due to the nonlinear dependence of the air–water interfacial adsorption coefficient on the aqueous concentration (see Equation 15). To test the hypothesis, we conduct an additional set of simulations where we reduce the inlet PFAS concentration by 1,000 times to 1 μg/L so that the air–water interfacial adsorption coefficient becomes essentially a constant (Equation 15); $K_{aw} = 4.250 \times 10^{-2}$ cm at 1 μg/L, which is almost identical to the maximum $K_{aw} = 4.251 \times 10^{-2}$ cm at zero aqueous concentration. As expected, linear adsorption almost eliminates the difference between the effective A_{aw} and the actual A_{aw} (<2.4%) (see Table 5). Finally, we note that the relative global mass conservation errors are below 1.5% in all simulations, which are sufficiently small to have any notable impact on PFAS transport in the simulated sand medium.

In addition to assessing the accessibility of the air–water interfaces by PFAS, the above analysis also has important implications for measuring A_{aw} from miscible displacement experiments using aqueous-phase interfacially active tracers. The difference between the estimated A_{aw} for the two concentrations 1 mg/L versus 1 μg/L indicates that A_{aw} may be overestimated if the tracer experiments are conducted for a concentration at which the air–water interfacial adsorption is nonlinear. To improve the accuracy of the estimated A_{aw}, lower tracer concentrations at which the air–water interfacial adsorption approaches a constant would be preferable (Brusseau, Lyu, et al., 2020). Furthermore, miscible displacement experiments often collect a limited number of pore volumes for the breakthrough curves due

to practical limitations. When long tailing is present due to strong nonequilibrium behaviors, not including the full long tailing of the measured breakthrough curves may underestimate the retardation factors and subsequently the A_{aw}.

While it is a common approach to compute A_{aw} by Equation 17 using the retardation factor obtained from the breakthrough curves via moment analysis, an alternative commonly used approach is to estimate A_{aw} via inverse modeling by fitting a one-dimensional (1D) advection-dispersion model to the measured breakthrough curve. When strong nonequilibrium behaviors are present, using an upscaled 1D transport model not fully capturing the complex nonequilibrium processes in the system may lead to uncertainties in the inversely estimated A_{aw}. Therefore, when strong nonequilibrium behaviors arise (e.g., at relatively lower water saturations), moment analysis may be a better approach for estimating A_{aw} because the moment-analysis-based retardation factor is independent of any nonequilibrium processes in the system (Valocchi, 1985).

5. Conclusion

We have developed a pore-scale model that represents a variety of PFAS retention and transport processes including the adsorption at bulk capillary and thin-water-film air–water interfaces as well as the mass-transfer processes between bulk capillary water and thin water films in water-unsaturated porous media (including advection, aqueous diffusion, and surface diffusion along the air–water interfaces). PFAS adsorption at the solid–water interfaces is also accounted for. Constrained by experimentally determined hydraulic parameters and air–water interfacial area data sets, we apply the pore-scale model to study how mass-transfer limitations between bulk capillary water and thin water films affect PFAS transport in a water-unsaturated sand medium. In particular, we focus on investigating two critical processes that have not been represented for PFAS transport in the literature—surface diffusion of the PFAS adsorbed at air–water interfaces and the disconnect of bulk capillary water as the water saturation in the soil medium decreases. Additionally, we also examine the impact of several other factors influencing the mass transfer between bulk capillary water and thin water films, including soil grain surface roughness, wetting conditions, and PFAS interfacial activity. The main findings are summarized below.

1. Adsorption at the air–water interfaces of the thin water films can contribute significantly to the retention of PFAS in water-unsaturated soil media, especially for soils with significant grain surface roughness and under field-relevant wetting conditions (e.g., $S_w < 0.5$). For the sand medium studied in the present work, adsorption at the thin-water-film air–water interfaces accounts for up to 75% and 84% of the total retention of PFOA and up to 88% and 91% for the total retention of PFOS, at $S_w = 0.3$ and $S_w = 0.5$, respectively.
2. Surface diffusion along the air–water interfaces is a critical process responsible for the transfer of PFAS mass between bulk capillary water and thin water films. Because of the greatly increased mass-transfer rate due to surface diffusion, PFAS in the bulk capillary water and thin water films inside each water-unsaturated pore body can be considered in chemical equilibrium. However, significant mass-transfer limitations still arise in the thin water films in the pore clusters where the bulk capillary water disconnects. The disconnect of bulk capillary water naturally occurs as the water saturation in a soil medium decreases, which can greatly increase the time scale of mass transfer between bulk capillary water and thin water films. The significant mass-transfer limitations in the thin water films strongly influence the transport of PFAS in water-unsaturated soil media, leading to early arrival and long tailing behaviors in the breakthrough curves.
3. While the mass-transfer limitations in the thin water films lead to strong nonequilibrium behaviors in the breakthrough curves, they do not appear to reduce the accessibility of thin-water-film air–water interfaces by PFAS. For the simulations conducted in the sand medium of the present work, the air–water interfaces in all of the thin water films were accessed by PFAS. It is important to point out that our moment analysis employed up to 5,000 pore volumes of the simulated breakthrough curves to compute the air–water interfacial area. However, miscible displacement experiments often collect a limited number of pore volumes for the breakthrough curves due to practical limitations, which may lead to an underestimated air–water interfacial area when long tailing is present due to strong nonequilibrium behaviors.
4. The mass-transfer limitations in the thin water films and the resulting nonequilibrium transport of PFAS are expected to be important processes controlling PFAS transport in the vadose zone. Natural soil media often have greater grain surface roughness than the sand medium examined in the present work (Jiang et al., 2020a), which may further increase the time scale of mass transfer in the thin water films. Additionally, the water saturations in our study (i.e., $S_w = 0.3$ and $S_w = 0.5$) are still relatively high for a sand medium. The disconnect of bulk capillary water may be more significant under the drier conditions that occur in the field (Anderson et al., 2022; Schaefer et al., 2022) and may substantially increase the mass-transfer limitations in thin water

films. These insights obtained from the pore-scale simulations need to be incorporated into an upscaled model to investigate the impact of potential mass transfer limitations in thin water films for field-scale applications. An upscaled model may be derived by volume averaging (e.g., Whitaker, 2013) or by adapting and parameterizing classic multi-domain model formulations widely used for modeling contaminant transport in heterogeneous aquifers such as the multi-rate mass transfer models (e.g., Chen & Wagenet, 1995, 1997; Haggerty & Gorelick, 1995) or two- or multi-domain models (e.g., Brusseau et al., 1989; Valocchi, 1990).

Finally, we point out two factors that may be further examined using our pore-network modeling framework. First, all of the simulations in the present work are conducted for a sand medium. But, the degree of disconnected bulk water and the morphology of thin water films at a given water saturation will be a function of the soil media, including their specific pore structures, grain surface wettability, and surface roughness. The thin-water-film mass-transfer processes and their impact on the overall PFAS transport behavior will likely vary for different soil media, which needs to be further investigated. Second, our simulations did not consider surface diffusion along the solid–water interfaces due to the negligible solid-phase adsorption capacity of the sand medium used in the present work. For porous media with greater solid-phase adsorption capacities, the surface diffusion of the adsorbed molecules along the solid surface may become important, as demonstrated by various prior studies in the literature of groundwater solute transport (e.g., Crittenden et al., 1986; Hutzler et al., 1986; Schaefer et al., 2021), gas transport in shales (e.g., Guo et al., 2018; Javadpour, 2009; Xiong et al., 2012), and water treatment technologies (e.g., Crittenden & Weber, 1978; Hand et al., 1983; Ma et al., 1996). The pore-network modeling framework can be extended to include this process by adding an additional mass flux between the pore bodies driven by surface diffusion of the adsorbed PFAS at the solid–water interfaces.

Notation

Subscript i	Pore body i
Subscript j	Pore body j
Subscript ij	Pore throat ij which connects pore bodies i and j
Superscript b	Bulk water
Superscript f	Thin water film
Subscript aw	Air–water interface
Subscript sw	Solid–water interface
a_{aw}	Air–water interfacial area in a pore body [L^2]
a_{sw}	Solid–water interfacial area in a pore body [L^2]
a_w^b	Cross-sectional area for aqueous diffusion in bulk capillary water in a pore throat
a_w^f	Cross-sectional area for aqueous diffusion in thin water films in a pore throat [L^2]
A_{aw}	Specific air–water interfacial area in the pore network [L^{-1}]
A_{sw}	Specific solid–water interfacial area in the pore network [L^{-1}]
A_{svl}	Hamaker constant [$M \cdot L^2 \cdot T^{-2}$]
c	PFAS concentration [$M \cdot L^{-3}$]
C	Representative PFAS concentration in the pore network [$M \cdot L^{-3}$]
d	Soil grain diameter [L]
D_0	Aqueous diffusion coefficient [$L^2 \cdot T^{-1}$]
D_{aw}	Surface diffusion coefficient [$L^2 \cdot T^{-1}$]
G	Water conductance in a pore throat [$L^4 \cdot T \cdot M^{-1}$]
h_{ad}	Thickness of absorptive thin water films on smooth surfaces [L]
h^f	Thickness of thin water films [L]
h_m	The first fitting parameter for computing the X_l [L]
k	The second fitting parameter for computing the X_l [-]
K_{aw}	Air–water interfacial adsorption coefficient [L]
K_{sw}	The first Freundlich isotherm parameter for solid–water interfacial adsorption $\left[L \cdot \left(L^{-3}\right)^{1-N_{sw}}\right]$
l_{ij}	Length of pore throat ij [L]
l_i^f	Length of thin water film between bulk water and the center of thin water films in each face of pore body i [L]
l_{ij}^f	Length of thin water films between pore bodies i and j [L]

L_{aw}^{f}	The total air–water interfacial length for surface diffusion between bulk capillary water and thin water films in each face of a cubic pore body [L]
L_{aw}^{f}	The total air–water interfacial length for surface diffusion along the thin-water-film air–water interfaces in a pore throat [L]
L_x	Length of the pore network [L]
N_{sw}	The second Freundlich isotherm parameter for solid–water interfacial adsorption [-]
p	Water pressure in a pore body [$M \cdot L^{-1} \cdot T^{-2}$]
p^c	Capillary pressure in a pore body [$M \cdot L^{-1} \cdot T^{-2}$]
p_{cr}^c	Threshold pressure in a pore body above which the bulk water is disconnected [$M \cdot L^{-1} \cdot T^{-2}$]
P^c	Domain-averaged capillary pressure in the pore network [$M \cdot L^{-1} \cdot T^{-2}$]
Pe	Péclet numbers at the pore-scale $\left[\left(L \cdot T^{-1}\right) \cdot L \cdot \left(L^2 \cdot T^{-1}\right)^{-1}\right]$
q	Water flux in a pore throat [$L^3 \cdot T^{-1}$]
r	Radius of inscribed sphere of a cubic pore body [L]
r_c	Radius of air–water menisci at the corners of a pore body [L]
r_e	Radius of air–water menisci at the edges of a pore body [L]
R_0	Retardation factor [-]
R_g	Universal gas constant [$M \cdot L^2 \cdot T^{-2} \cdot K^{-1}$]
s	Water saturation in a pore body [$L^3 \cdot L^{-3}$]
S_w	Domain-averaged water saturation in the pore network [$L^3 \cdot L^{-3}$]
T	Temperature [K]
v_p	Domain-averaged pore water velocity in the pore network [$L \cdot T^{-1}$]
V	Volume of a pore body [L^3]
X	Surface roughness factor [-]
X_h	Amplification factor for the increase of thin-water-film thickness on rough surfaces [-]
X_l	Amplification factor for the increase of thin-water-film air–water interfacial area on rough surfaces[-]
α	The first fitting parameter of Szyszkowski model [L^{-3}]
β	The second fitting parameter of Szyszkowski model [-]
δ	Boolean function to account for the removal of bulk water conductance in a pore throat where the bulk water is disconnected [-]
ϵ_{μ_2}	Relative difference in second central moment [-]
θ	Domain-averaged water content of a pore network [$L^3 \cdot L^{-3}$]
μ	Water viscosity [$M \cdot L^{-1} \cdot T^{-1}$]
μ_1	The first central moment [-]
μ_2	The second central moment [-]
σ	Surface tension [$M \cdot T^{-2}$]
σ_0	Surface tension in the absence of PFAS [$M \cdot T^{-2}$]

Data Availability Statement

All the data sets used in the present study are included in the manuscript and its supporting information, tables, and/or figures. These data together with the model simulation output used to generate the figures in the manuscript and its supplementary files are available at https://doi.org/10.5281/zenodo.7604634.

Acknowledgments
This work was in part supported by the Water, Environmental, and Energy Solutions (WEES) at the University of Arizona, and the National Science Foundation (2023351 and 2237015).

References

Adamson, D. T., Nickerson, A., Kulkarni, P. R., Higgins, C. P., Popovic, J., Field, J., et al. (2020). Mass-based, field-scale demonstration of PFAS retention within AFFF-associated source areas. *Environmental Science and Technology*, *54*(24), 15768–15777. https://doi.org/10.1021/acs.est.0c04472

Anderson, R. H., Adamson, D. T., & Stroo, H. F. (2019). Partitioning of poly-and perfluoroalkyl substances from soil to groundwater within aqueous film-forming foam source zones. *Journal of Contaminant Hydrology*, *220*, 59–65. https://doi.org/10.1016/j.jconhyd.2018.11.011

Anderson, R. H., Feild, J. B., Dieffenbach-Carle, H., Elsharnouby, O., & Krebs, R. K. (2022). Assessment of PFAS in collocated soil and porewater samples at an AFFF-impacted source zone: Field-scale validation of suction lysimeters. *Chemosphere*, *308*, 136247. https://doi.org/10.1016/j.chemosphere.2022.136247

Araujo, J. B., & Brusseau, M. L. (2020). Assessing XMT-measurement variability of air-water interfacial areas in natural porous media. *Water Resources Research*, *56*(1), e2019WR025470. https://doi.org/10.1029/2019wr025470

Araujo, J. B., Mainhagu, J., & Brusseau, M. L. (2015). Measuring air–water interfacial area for soils using the mass balance surfactant-tracer method. *Chemosphere*, *134*, 199–202. https://doi.org/10.1016/j.chemosphere.2015.04.035

Bijeljic, B., & Blunt, M. J. (2006). Pore-scale modeling and continuous time random walk analysis of dispersion in porous media. *Water Resources Research*, *42*(1). https://doi.org/10.1029/2005wr004578

Bijeljic, B., Muggeridge, A. H., & Blunt, M. J. (2004). Pore-scale modeling of longitudinal dispersion. *Water Resources Research*, *40*(11). https://doi.org/10.1029/2004wr003567

Blunt, M. J. (2001). Flow in porous media—Pore-network models and multiphase flow. *Current Opinion in Colloid & Interface Science*, *6*(3), 197–207. https://doi.org/10.1016/s1359-0294(01)00084-x

Broadbent, S. R., & Hammersley, J. M. (1957). Percolation processes: I. Crystals and mazes. *Mathematical Proceedings of the Cambridge Philosophical Society*, *53*(3), 629–641. https://doi.org/10.1017/s0305004100032680

Brusseau, M. L. (2018). Assessing the potential contributions of additional retention processes to PFAS retardation in the subsurface. *Science of the Total Environment*, *613*, 176–185. https://doi.org/10.1016/j.scitotenv.2017.09.065

Brusseau, M. L. (2020). Simulating PFAS transport influenced by rate-limited multi-process retention. *Water Research*, *168*, 115179. https://doi.org/10.1016/j.watres.2019.115179

Brusseau, M. L., Anderson, R. H., & Guo, B. (2020). PFAS concentrations in soils: Background levels versus contaminated sites. *Science of the Total Environment*, *740*, 140017. https://doi.org/10.1016/j.scitotenv.2020.140017

Brusseau, M. L., & Guo, B. (2021). Air-water interfacial areas relevant for transport of per and poly-fluoroalkyl substances. *Water Research*, *207*, 117785. https://doi.org/10.1016/j.watres.2021.117785

Brusseau, M. L., Jessup, R., & Rao, P. (1989). Modeling the transport of solutes influenced by multiprocess nonequilibrium. *Water Resources Research*, *25*(9), 1971–1988. https://doi.org/10.1029/wr025i009p01971

Brusseau, M. L., Khan, N., Wang, Y., Yan, N., Van Glubt, S., & Carroll, K. C. (2019). Nonideal transport and extended elution tailing of PFOS in soil. *Environmental Science and Technology*, *53*(18), 10654–10664. https://doi.org/10.1021/acs.est.9b02343

Brusseau, M. L., Lyu, Y., Yan, N., & Guo, B. (2020). Low-concentration tracer tests to measure air-water interfacial area in porous media. *Chemosphere*, *250*, 126305. https://doi.org/10.1016/j.chemosphere.2020.126305

Brusseau, M. L., Peng, S., Schnaar, G., & Costanza-Robinson, M. S. (2006). Relationships among air-water interfacial area, capillary pressure, and water saturation for a sandy porous medium. *Water Resources Research*, *42*(3). https://doi.org/10.1029/2005wr004058

Brusseau, M. L., Peng, S., Schnaar, G., & Murao, A. (2007). Measuring air-water interfacial areas with X-ray microtomography and interfacial partitioning tracer tests. *Environmental Science and Technology*, *41*(6), 1956–1961. https://doi.org/10.1021/es061474m

Brusseau, M. L., & Van Glubt, S. (2019). The influence of surfactant and solution composition on pfas adsorption at fluid-fluid interfaces. *Water Research*, *161*, 17–26. https://doi.org/10.1016/j.watres.2019.05.095

Brusseau, M. L., Yan, N., Van Glubt, S., Wang, Y., Chen, W., Lyu, Y., et al. (2019). Comprehensive retention model for PFAS transport in subsurface systems. *Water Research*, *148*, 41–50. https://doi.org/10.1016/j.watres.2018.10.035

Celia, M. A., Reeves, P. C., & Ferrand, L. A. (1995). Recent advances in pore scale models for multiphase flow in porous media. *Reviews of Geophysics*, *33*(S2), 1049–1057. https://doi.org/10.1029/95rg00248

Chen, S., Qin, C., & Guo, B. (2020). Fully implicit dynamic pore-network modeling of two-phase flow and phase change in porous media. *Water Resources Research*, *56*(11), e2020WR028510. https://doi.org/10.1029/2020wr028510

Chen, W., & Wagenet, R. J. (1995). Solute transport in porous media with sorption-site heterogeneity. *Environmental Science and Technology*, *29*(11), 2725–2734. https://doi.org/10.1021/es00011a005

Chen, W., & Wagenet, R. J. (1997). Description of atrazine transport in soil with heterogeneous nonequilibrium sorption. *Soil Science Society of America Journal*, *61*(2), 360–371. https://doi.org/10.2136/sssaj1997.03615995006100020003x

Costanza, J., Arshadi, M., Abriola, L. M., & Pennell, K. D. (2019). Accumulation of PFOA and PFOS at the air–water interface. *Environmental Science and Technology Letters*, *6*(8), 487–491. https://doi.org/10.1021/acs.estlett.9b00355

Costanza-Robinson, M. S., & Brusseau, M. L. (2002). Air-water interfacial areas in unsaturated soils: Evaluation of interfacial domains. *Water Resources Research*, *38*(10), 13–21. https://doi.org/10.1029/2001wr000738

Crittenden, J. C., Hutzler, N. J., Geyer, D. G., Oravitz, J. L., & Friedman, G. (1986). Transport of organic compounds with saturated groundwater flow: Model development and parameter sensitivity. *Water Resources Research*, *22*(3), 271–284. https://doi.org/10.1029/wr022i003p00271

Crittenden, J. C., & Weber, W. J., Jr. (1978). Predictive model for design of fixed-bed adsorbers: Parameter estimation and model development. *Journal of the Environmental Engineering Division*, *104*(2), 185–197. https://doi.org/10.1061/jeegav.0000743

Dalla, E., Hilpert, M., & Miller, C. T. (2002). Computation of the interfacial area for two-fluid porous medium systems. *Journal of Contaminant Hydrology*, *56*(1–2), 25–48. https://doi.org/10.1016/s0169-7722(01)00202-9

Dauchy, X., Boiteux, V., Colin, A., Hémard, J., Bach, C., Rosin, C., & Munoz, J.-F. (2019). Deep seepage of per-and polyfluoroalkyl substances through the soil of a firefighter training site and subsequent groundwater contamination. *Chemosphere*, *214*, 729–737. https://doi.org/10.1016/j.chemosphere.2018.10.003

Filipovic, M., Woldegiorgis, A., Norström, K., Bibi, M., Lindberg, M., & Österås, A.-H. (2015). Historical usage of aqueous film forming foam: A case study of the widespread distribution of perfluoroalkyl acids from a military airport to groundwater, lakes, soils and fish. *Chemosphere*, *129*, 39–45. https://doi.org/10.1016/j.chemosphere.2014.09.005

Frisch, H., & Hammersley, J. (1963). Percolation processes and related topics. *Journal of the Society for Industrial and Applied Mathematics*, *11*(4), 894–918. https://doi.org/10.1137/0111066

Guo, B., Ma, L., & Tchelepi, H. A. (2018). Image-based micro-continuum model for gas flow in organic-rich shale rock. *Advances in Water Resources*, *122*, 70–84. https://doi.org/10.1016/j.advwatres.2018.10.004

Guo, B., Zeng, J., & Brusseau, M. L. (2020). A mathematical model for the release, transport, and retention of per-and polyfluoroalkyl substances (PFAS) in the vadose zone. *Water Resources Research*, *56*(2), e2019WR026667. https://doi.org/10.1029/2019wr026667

Guo, B., Zeng, J., Brusseau, M. L., & Zhang, Y. (2022). A screening model for quantifying PFAS leaching in the vadose zone and mass discharge to groundwater. *Advances in Water Resources*, *160*, 104102. https://doi.org/10.1016/j.advwatres.2021.104102

Haggerty, R., & Gorelick, S. M. (1995). Multiple-rate mass transfer for modeling diffusion and surface reactions in media with pore-scale heterogeneity. *Water Resources Research*, *31*(10), 2383–2400. https://doi.org/10.1029/95wr10583

Hand, D. W., Crittenden, J. C., & Thacker, W. E. (1983). User-oriented batch reactor solutions to the homogeneous surface diffusion model. *Journal of Environmental Engineering*, *109*(1), 82–101. https://doi.org/10.1061/(asce)0733-9372(1983)109:1(82)

Hasan, S., Joekar-Niasar, V., Karadimitriou, N. K., & Sahimi, M. (2019). Saturation dependence of non-fickian transport in porous media. *Water Resources Research*, *55*(2), 1153–1166. https://doi.org/10.1029/2018wr023554

Higgins, C. P., & Luthy, R. G. (2006). Sorption of perfluorinated surfactants on sediments. *Environmental Science and Technology*, *40*(23), 7251–7256. https://doi.org/10.1021/es061000n

Hutzler, N. J., Crittenden, J. C., Gierke, J. S., & Johnson, A. S. (1986). Transport of organic compounds with saturated groundwater flow: Experimental results. *Water Resources Research*, *22*(3), 285–295. https://doi.org/10.1029/wr022i003p00285

Iwamatsu, M., & Horii, K. (1996). Capillary condensation and adhesion of two wetter surfaces. *Journal of Colloid and Interface Science*, *182*(2), 400–406. https://doi.org/10.1006/jcis.1996.0480

Javadpour, F. (2009). Nanopores and apparent permeability of gas flow in mudrocks (shales and siltstone). *Journal of Canadian Petroleum Technology*, *48*(08), 16–21. https://doi.org/10.2118/09-08-16-da

Ji, Y., Yan, N., Brusseau, M. L., Guo, B., Zheng, X., Dai, M., & Li, X. (2021). Impact of a hydrocarbon surfactant on the retention and transport of perfluorooctanoic acid in saturated and unsaturated porous media. *Environmental Science and Technology*, *55*(15), 10480–10490. https://doi.org/10.1021/acs.est.1c01919

Jiang, H., Guo, B., & Brusseau, M. L. (2020a). Characterization of the micro-scale surface roughness effect on immiscible fluids and interfacial areas in porous media using the measurements of interfacial partitioning tracer tests. *Advances in Water Resources*, *146*, 103789. https://doi.org/10.1016/j.advwatres.2020.103789

Jiang, H., Guo, B., & Brusseau, M. L. (2020b). Pore-scale modeling of fluid-fluid interfacial area in variably saturated porous media containing microscale surface roughness. *Water Resources Research*, *56*(1), e2019WR025876. https://doi.org/10.1029/2019wr025876

Joekar-Niasar, V., Hassanizadeh, S. M., & Dahle, H. (2010). Non-equilibrium effects in capillarity and interfacial area in two-phase flow: Dynamic pore-network modelling. *Journal of Fluid Mechanics*, *655*, 38–71. https://doi.org/10.1017/s0022112010000704

Karakashev, S. I., & Ivanova, D. S. (2010). Thin liquid film drainage: Ionic vs. non-ionic surfactants. *Journal of Colloid and Interface Science*, *343*(2), 584–593. https://doi.org/10.1016/j.jcis.2009.11.065

Kibbey, T. C., & Chen, L. (2012). A pore network model study of the fluid-fluid interfacial areas measured by dynamic-interface tracer depletion and miscible displacement water phase advective tracer methods. *Water Resources Research*, *48*(10). https://doi.org/10.1029/2012wr011862

Li, L., Peters, C. A., & Celia, M. A. (2006). Upscaling geochemical reaction rates using pore-scale network modeling. *Advances in Water Resources*, *29*(9), 1351–1370. https://doi.org/10.1016/j.advwatres.2005.10.011

Lyu, X., Liu, X., Sun, Y., Gao, B., Ji, R., Wu, J., & Xue, Y. (2020). Importance of surface roughness on perfluorooctanoic acid (PFOA) transport in unsaturated porous media. *Environmental Pollution*, *266*, 115343. https://doi.org/10.1016/j.envpol.2020.115343

Lyu, Y., Brusseau, M. L., Chen, W., Yan, N., Fu, X., & Lin, X. (2018). Adsorption of PFOA at the air–water interface during transport in unsaturated porous media. *Environmental Science and Technology*, *52*(14), 7745–7753. https://doi.org/10.1021/acs.est.8b02348

Ma, Z., Whitley, R., & Wang, N.-H. (1996). Pore and surface diffusion in multicomponent adsorption and liquid chromatography systems. *AIChE Journal*, *42*(5), 1244–1262. https://doi.org/10.1002/aic.690420507

Mehmani, Y., Oostrom, M., & Balhoff, M. T. (2014). A streamline splitting pore-network approach for computationally inexpensive and accurate simulation of transport in porous media. *Water Resources Research*, *50*(3), 2488–2517. https://doi.org/10.1002/2013wr014984

Mehmani, Y., & Tchelepi, H. A. (2017). Minimum requirements for predictive pore-network modeling of solute transport in micromodels. *Advances in Water Resources*, *108*, 83–98. https://doi.org/10.1016/j.advwatres.2017.07.014

Oostrom, M., Mehmani, Y., Romero-Gomez, P., Tang, Y., Liu, H., Yoon, H., et al. (2016). Pore-scale and continuum simulations of solute transport micromodel benchmark experiments. *Computational Geosciences*, *20*(4), 857–879. https://doi.org/10.1007/s10596-014-9424-0

Or, D., & Tuller, M. (1999). Liquid retention and interfacial area in variably saturated porous media: Upscaling from single-pore to sample-scale model. *Water Resources Research*, *35*(12), 3591–3605. https://doi.org/10.1029/1999wr900262

Peng, S., & Brusseau, M. L. (2005). Impact of soil texture on air-water interfacial areas in unsaturated sandy porous media. *Water Resources Research*, *41*(3). https://doi.org/10.1029/2004wr003233

Porter, M. L., Schaap, M. G., & Wildenschild, D. (2009). Lattice-Boltzmann simulations of the capillary pressure–saturation–interfacial area relationship for porous media. *Advances in Water Resources*, *32*(11), 1632–1640. https://doi.org/10.1016/j.advwatres.2009.08.009

Qin, C.-Z., & Hassanizadeh, S. M. (2015). Pore-network modeling of solute transport and biofilm growth in porous media. *Transport in Porous Media*, *110*(3), 345–367. https://doi.org/10.1007/s11242-015-0546-1

Qin, C.-Z., Hassanizadeh, S. M., & Ebigbo, A. (2016). Pore-scale network modeling of microbially induced calcium carbonate precipitation: Insight into scale dependence of biogeochemical reaction rates. *Water Resources Research*, *52*(11), 8794–8810. https://doi.org/10.1002/2016wr019128

Qin, C.-Z., & van Brummelen, H. (2019). A dynamic pore-network model for spontaneous imbibition in porous media. *Advances in Water Resources*, *133*, 103420. https://doi.org/10.1016/j.advwatres.2019.103420

Quinnan, J., Rossi, M., Curry, P., Lupo, M., Miller, M., Korb, H., & Hasbrouck, K. (2021). Application of pfas-mobile lab to support adaptive characterization and flux-based conceptual site models at AFFF releases. *Remediation Journal*, *31*(3), 7–26. https://doi.org/10.1002/rem.21680

Raoof, A., & Hassanizadeh, S. (2013). Saturation-dependent solute dispersivity in porous media: Pore-scale processes. *Water Resources Research*, *49*(4), 1943–1951. https://doi.org/10.1002/wrcr.20152

Raoof, A., Hassanizadeh, S. M., & Leijnse, A. (2010). Upscaling transport of adsorbing solutes in porous media: Pore-network modeling. *Vadose Zone Journal*, *9*(3), 624–636. https://doi.org/10.2136/vzj2010.0026

Reeves, P. C., & Celia, M. A. (1996). A functional relationship between capillary pressure, saturation, and interfacial area as revealed by a pore-scale network model. *Water Resources Research*, *32*(8), 2345–2358. https://doi.org/10.1029/96wr01105

Schaefer, C. E., Culina, V., Nguyen, D., & Field, J. (2019). Uptake of poly-and perfluoroalkyl substances at the air–water interface. *Environmental Science and Technology*, *53*(21), 12442–12448. https://doi.org/10.1021/acs.est.9b04008

Schaefer, C. E., Drennan, D., Nickerson, A., Maizel, A., & Higgins, C. P. (2021). Diffusion of perfluoroalkyl acids through clay-rich soil. *Journal of Contaminant Hydrology*, *241*, 103814. https://doi.org/10.1016/j.jconhyd.2021.103814

Schaefer, C. E., Drennan, D. M., Tran, D. N., Garcia, R., Christie, E., Higgins, C. P., & Field, J. A. (2019). Measurement of aqueous diffusivities for perfluoroalkyl acids. *Journal of Environmental Engineering*, *145*(11), 06019006. https://doi.org/10.1061/(asce)ee.1943-7870.0001585

Schaefer, C. E., Lavorgna, G. M., Lippincott, D. R., Nguyen, D., Christie, E., Shea, S., et al. (2022). A field study to assess the role of air-water interfacial sorption on PFAS leaching in an AFFF source area. *Journal of Contaminant Hydrology*, *248*, 104001. https://doi.org/10.1016/j.jconhyd.2022.104001

Silva, J. A., Martin, W. A., Johnson, J. L., & McCray, J. E. (2019). Evaluating air-water and NAPL-water interfacial adsorption and retention of perfluorocarboxylic acids within the vadose zone. *Journal of Contaminant Hydrology*, *223*, 103472. https://doi.org/10.1016/j.jconhyd.2019.03.004

Stoyanov, S. D., & Denkov, N. D. (2001). Role of surface diffusion for the drainage and hydrodynamic stability of thin liquid films. *Langmuir*, *17*(4), 1150–1156. https://doi.org/10.1021/la001214x

Stults, J. F., Choi, Y. J., Schaefer, C. E., Illangasekare, T. H., & Higgins, C. P. (2022). *Estimation of transport parameters of perfluoroalkyl acids (PFAAs) in unsaturated porous media: Critical experimental and modeling improvements*. Environmental Science and Technology.

Thompson, K. E. (2002). Pore-scale modeling of fluid transport in disordered fibrous materials. *AIChE Journal*, *48*(7), 1369–1389. https://doi.org/10.1002/aic.690480703

Tokunaga, T. K. (2011). Physicochemical controls on adsorbed water film thickness in unsaturated geological media. *Water Resources Research*, *47*(8). https://doi.org/10.1029/2011wr010676

Tuller, M., & Or, D. (2001). Hydraulic conductivity of variably saturated porous media: Film and corner flow in angular pore space. *Water Resources Research*, *37*(5), 1257–1276. https://doi.org/10.1029/2000wr900328

Valkovska, D. S., & Danov, K. D. (2000). Determination of bulk and surface diffusion coefficients from experimental data for thin liquid film drainage. *Journal of Colloid and Interface Science*, *223*(2), 314–316. https://doi.org/10.1006/jcis.1999.6657

Valkovska, D. S., & Danov, K. D. (2001). Influence of ionic surfactants on the drainage velocity of thin liquid films. *Journal of Colloid and Interface Science*, *241*(2), 400–412. https://doi.org/10.1006/jcis.2001.7757

Valocchi, A. J. (1985). Validity of the local equilibrium assumption for modeling sorbing solute transport through homogeneous soils. *Water Resources Research*, *21*(6), 808–820. https://doi.org/10.1029/wr021i006p00808

Valocchi, A. J. (1990). Use of temporal moment analysis to study reactive solute transport in aggregated porous media. *Geoderma*, *46*(1–3), 233–247. https://doi.org/10.1016/0016-7061(90)90017-4

Vanapalli, S., Sillers, W., & Fredlund, M. (1998). The meaning and relevance of residual state to unsaturated soils. In *51st Canadian Geotechnical Conference* (pp. 4–7).

Van Glubt, S., Brusseau, M. L., Yan, N., Huang, D., Khan, N., & Carroll, K. C. (2021). Column versus batch methods for measuring PFOS and PFOA sorption to geomedia. *Environmental Pollution*, *268*, 115917. https://doi.org/10.1016/j.envpol.2020.115917

Wan, J., & Tokunaga, T. K. (1997). Film straining of colloids in unsaturated porous media: Conceptual model and experimental testing. *Environmental Science and Technology*, *31*(8), 2413–2420. https://doi.org/10.1021/es970017q

Weber, A. K., Barber, L. B., LeBlanc, D. R., Sunderland, E. M., & Vecitis, C. D. (2017). Geochemical and hydrologic factors controlling subsurface transport of poly-and perfluoroalkyl substances, Cape Cod, Massachusetts. *Environmental Science and Technology*, *51*(8), 4269–4279. https://doi.org/10.1021/acs.est.6b05573

Wei, C., Song, X., Wang, Q., & Hu, Z. (2017). Sorption kinetics, isotherms and mechanisms of PFOS on soils with different physicochemical properties. *Ecotoxicology and Environmental Safety*, *142*, 40–50. https://doi.org/10.1016/j.ecoenv.2017.03.040

Weishaupt, K., & Helmig, R. (2021). A dynamic and fully implicit non-isothermal, two-phase, two-component pore-network model coupled to single-phase free flow for the pore-scale description of evaporation processes. *Water Resources Research*, *57*(4), e2020WR028772. https://doi.org/10.1029/2020wr028772

Weishaupt, K., Koch, T., & Helmig, R. (2022). A fully implicit coupled pore-network/free-flow model for the pore-scale simulation of drying processes. *Drying Technology*, *40*(4), 697–718. https://doi.org/10.1080/07373937.2021.1955706

Whitaker, S. (2013). *The method of volume averaging* (Vol. 13). Springer Science and Business Media.

Wilkinson, D., & Willemsen, J. F. (1983). Invasion percolation: A new form of percolation theory. *Journal of Physics A: Mathematical and General*, *16*(14), 3365–3376. https://doi.org/10.1088/0305-4470/16/14/028

Xiao, F., Simcik, M. F., Halbach, T. R., & Gulliver, J. S. (2015). Perfluorooctane sulfonate (PFOS) and perfluorooctanoate (PFOA) in soils and groundwater of a US metropolitan area: Migration and implications for human exposure. *Water Research*, *72*, 64–74. https://doi.org/10.1016/j.watres.2014.09.052

Xiong, X., Devegowda, D., Michel, G., Sigal, R. F., & Civan, F. (2012). A fully-coupled free and adsorptive phase transport model for shale gas reservoirs including non-Darcy flow effects. In *SPE Annual Technical Conference and Exhibition*.

Yang, X., Mehmani, Y., Perkins, W. A., Pasquali, A., Schönherr, M., Kim, K., et al. (2016). Intercomparison of 3D pore-scale flow and solute transport simulation methods. *Advances in Water Resources*, *95*, 176–189. https://doi.org/10.1016/j.advwatres.2015.09.015

Zeng, J., Brusseau, M. L., & Guo, B. (2021). Model validation and analyses of parameter sensitivity and uncertainty for modeling long-term retention and leaching of PFAS in the vadose zone. *Journal of Hydrology*, *603*, 127172. https://doi.org/10.1016/j.jhydrol.2021.127172

Zheng, W., Yu, X., & Jin, Y. (2015). Considering surface roughness effects in a triangular pore space model for unsaturated hydraulic conductivity. *Vadose Zone Journal*, *14*(7). https://doi.org/10.2136/vzj2014.09.0121